










# Maternal immune activation leads to defective brain–blood vessels and intracerebral hemorrhages in male offspring

Marco Rasile<sup>1,2</sup> , Eliana Lauranzano<sup>2</sup> , Elisa Faggiani<sup>2</sup>, Margherita M Ravanelli<sup>1,2</sup> , Federico S Colombo<sup>2</sup>, Filippo Mirabella<sup>1,2</sup>, Irene Corradini<sup>2,3</sup> , Maria L Malosio<sup>2,3</sup>, Antonella Borreca<sup>2,3</sup> , Elisa Focchi<sup>3</sup>, Davide Pozzi<sup>1,2</sup>, Toni Giorgino<sup>4</sup> , Isabella Barajon<sup>1,2</sup> & Michela Matteoli<sup>1,3,\*</sup> 

## Abstract

Intracerebral hemorrhages are recognized risk factors for neurodevelopmental disorders and represent early biomarkers for cognitive dysfunction and mental disability, but the pathways leading to their occurrence are not well defined. We report that a single intrauterine exposure of the immunostimulant Poly I:C to pregnant mice at gestational day 9, which models a prenatal viral infection and the consequent maternal immune activation, induces the defective formation of brain vessels and causes intracerebral hemorrhagic events, specifically in male offspring. We demonstrate that maternal immune activation promotes the production of the TGF- $\beta$ 1 active form and the consequent enhancement of pSMAD1-5 in males' brain endothelial cells. TGF- $\beta$ 1, in combination with IL-1 $\beta$ , reduces the endothelial expression of CD146 and claudin-5, alters the endothelium–pericyte interplay resulting in low pericyte coverage, and increases hemorrhagic events in the adult offspring. By showing that exposure to Poly I:C at the beginning of fetal cerebral angiogenesis results in sex-specific alterations of brain vessels, we provide a mechanistic framework for the association between intragaventric infections and anomalies of the neural vasculature, which may contribute to neuropsychiatric disorders.

**Keywords** CD146; intracerebral hemorrhages; MIA; NVU; sex dimorphism

**Subject Categories** Immunology; Neuroscience

**DOI** 10.15252/embj.2022111192 | Received 16 March 2022 | Revised 21

September 2022 | Accepted 27 September 2022 | Published online 31 October 2022

The EMBO Journal (2022) 41: e111192

## Introduction

The proper formation of the neurovascular unit (NVU) ensures the segregation of the brain parenchyma from blood-borne circulating

molecules, preventing vasogenic edema, passage of harmful substances, and microbe invasion (Saunders *et al*, 2012; Goasdoué *et al*, 2017). Furthermore, a healthy NVU can rapidly respond and adapt to the metabolic demands of neurons, allowing the transfer of nutrient molecules and oxygen as needed (Sweeney *et al*, 2019). Under this respect, the formation, maturation, and maintenance of an intact brain vasculature are crucial processes for brain homeostasis and proper neuronal functioning.

In mice, endothelial cells start the formation of the brain–blood vessels around embryonic day 9.5 (E9.5) (Mancuso *et al*, 2008). The subsequent maturation of interendothelial tight junctions (TJ) and recruitment of pericytes by E10 (Armulik *et al*, 2010), and astrocytes a week later (Daneman *et al*, 2010), allow the completion of vessel sealing. Seal failure, regardless of its origin, is an early marker of cognitive dysfunction and mental disability (Moretti *et al*, 2015; Bell *et al*, 2019; Nation *et al*, 2019), with prenatal and perinatal cerebral bleedings being associated with autism (Gardener *et al*, 2011), depression (Preti *et al*, 2000), cerebral palsy (Gardner, 2005), and bipolar disorder (Kinney *et al*, 1998). Moreover, perinatal brain hemorrhages are a recognized risk factor for schizophrenia (Rosanoff *et al*, 1934; Torrey *et al*, 1975), a condition that can be modeled by prenatal injections of pro-hemorrhagic agents in rodents (Mirendil *et al*, 2015). Although anomalies in the NVU formation can result in long-lasting consequences and impairments in brain maturation, the origins of these anomalies are still not fully clarified.

Extensive epidemiological evidence links intragaventric infections to the later occurrence of neuropsychiatric disorders in the progeny (Knuesel *et al*, 2014; Brown & Meyer, 2018; Al-Haddad *et al*, 2019; Lydholm *et al*, 2019; López-Aranda *et al*, 2021) and identifies influenza virus infection as one of the most well-replicated risk factors for schizophrenia (Brown & Derkits, 2010). In recent years, the maternal immune activation (MIA) model has provided insightful data, demonstrating that sterile inflammation—mostly induced by the means of lipopolysaccharide (LPS) or polyinosinic:polycytidylic acid (Poly I:C) injections during pregnancy—is sufficient to induce

1 Department of Biomedical Sciences, Humanitas University, Pieve Emanuele, Italy

2 IRCCS Humanitas Clinical and Research Center, Rozzano, Italy

3 Institute of Neuroscience (IN-CNR), National Research Council of Italy, Milan, Italy

4 Institute of Biophysics (IBF-CNR), National Research Council of Italy, Milan, Italy

\*Corresponding author. Tel: +39 02 8224 5254; E-mail: michela.matteoli@hunimed.eu

gender-specific autistic-like and schizophrenia-like behaviors in the offspring (Corradini *et al*, 2018; Hui *et al*, 2018; Al-Haddad *et al*, 2019). These observations led us to test the hypothesis that early prenatal immune activation may impact brain–blood vessel formation and function. We report a male-specific alteration of the early endothelium–pericytes interplay in MIA offspring, which results in defective barrier sealing and intracerebral hemorrhages.

## Results

### MIA offspring show a sex-specific remodeling of brain vessels leading to increased permeability

We aimed to establish whether Poly I:C-induced maternal immune activation can divert the developmental trajectory of brain vessels and the blood–brain barrier (BBB) formation in the offspring. To this aim, a single Poly I:C i.p. injection (2 mg/kg—Appendix Fig S1A) was given to pregnant mice at gestational day 9 (GD9), which corresponds to the beginning of brain angiogenesis (Mancuso *et al*, 2008). Morphological and functional analyses of the brain vasculature were performed in male and female offspring at different time points, from GD9 to P90 (Appendix Fig S1B). As already shown, this experimental protocol leads to a significant increase in IL-6 in the plasma of treated dams (Corradini *et al*, 2018). Consistently, ELISA analysis of IL-1 $\beta$ , IL-6, and IL-1RA—performed on the amniotic fluids collected from E17 embryos—showed a significant increase in IL-6 in the intrauterine environment of Poly I:C-treated offspring versus the control (Appendix Fig S1C), confirming the induction of sterile inflammation.

To assess if Poly I:C-induced inflammation leads to an altered vascular geometry in the offspring, we analyzed the cerebral vessels of intravenously DiI-labeled P90 males and females. The 3D rendering of the cortical vasculature revealed that Poly I:C males (Fig 1A and B), but not females (Fig 1C and D), display a higher number of vessels per area analyzed, which accounts for a longer and more branched vascular tree (Fig 1A and B). Moreover, while males present a significant reduction in the mean vessel's diameter, females show the opposite phenotype coupled with accompanied by an increased length of the branches (Fig 1A–D). These results were confirmed by the vessel geometry analysis performed in CD31-stained male brain slices (Appendix Fig S2A and B). Thus, MIA consequent to injection of low-dosage Poly I:C at GD9 causes a sex-specific remodeling of the brain vessels in the offspring.

To assess the functional integrity of the brain–blood vessels, Poly I:C and vehicle-treated offspring were tested through Evans blue (EB) injections at P30 and P90. EB is a small dye that binds to the 67 kDa plasma protein albumin which, in the presence of an intact barrier, is prevented from entering the brain parenchyma (Yao *et al*, 2018). After EB administration, mice were perfused with the same amounts of saline solution, and EB in the brain parenchyma was quantified by absorbance at 620 nm, a wavelength far from the one of hemoglobin (i.e., 540–576 nm) (Liu *et al*, 2012). An increase in EB extravasation was detected in male brains at both P30 (Fig 1E) and P90 (Fig 1F), while no sealing defect was detectable in females (Fig 1I and J). EB and albumin extravasation in Poly I:C males were also detectable by microscopy analyses (Appendix Fig S2C and D).

To define the molecular basis of the barrier leakiness, we analyzed by western blotting the expression of the main junctional proteins of the brain–blood vessels—claudin-5, zonula occludens-1 (ZO-1) and occludin—in the offspring cerebral cortex tissues at P90. Male offspring showed a significantly reduced expression of claudin-5 and ZO-1 (Fig 1G and H) in the absence of differences for occludin (Appendix Fig S2E). No significant difference in tight junction protein expression was found in females (Fig 1K and L; Appendix Fig S2B). Immunofluorescence staining for claudin-5 and ZO-1 confirmed a reduced expression and a disorganized morphology of the two proteins in brain sections from P90 male MIA offspring (Fig 1M–Q).

To test if the BBB breakdown observed in the Poly I:C male offspring was dependent on the time of the MIA insult, we compared the effects produced by Poly I:C injection at GD9-MIA or P20 (Fig 1R and S). In the latter condition, male mice were injected with Poly I:C at P20—when most of the angiogenesis process in the brain has ended (Coelho-Santos & Shih, 2020)—and examined at P90 (Fig 1S). Results indicated that, when challenged at P20, P90 mice did not show EB leakage (Fig 1T), or variations in the expression of claudin-5 (Fig 1U), ZO-1 (Fig 1V), or occludin (Appendix Fig S2G). These data indicate that male offspring, differently from their female siblings, display a looser barrier and defective junctional proteins when exposed to MIA at early gestational stages.

### MIA offspring display a sex-specific altered expression of vascular and inflammatory genes

The observation that the BBB breakdown occurs in males upon Poly I:C injection at GD9, but not P20, points to the *in utero* developmental period as the sensitive time window for the MIA effect in a sex-specific manner. Since the process of cerebral vasculogenesis and angiogenesis is orchestrated by a precise time-dependent expression of specific molecular players, we hypothesized that MIA may disrupt the genetic program of cerebrovascular development in a gender-specific manner. We thus performed a temporal gene expression analysis of a panel of crucial molecular determinants for BBB formation in male and female tissues. Examined gene transcripts included platelet endothelial cell adhesion molecule (Pecam1), which encodes for CD31, a transmembrane homophilic receptor highly expressed by ECs; CD248, a PC marker of embryonic neovascularization (Virgintino *et al*, 2007); vascular endothelial growth factor A (VEGFa), which largely affects EC properties including increasing vascular permeability, angiogenesis, cell migration and inhibiting apoptosis (Mackenzie & Ruhrberg, 2012); platelet-derived growth factor subunit B (PDGFb), an essential mediator of PC recruitment (Bell *et al*, 2010); transforming growth factor beta (TGF- $\beta$ ), a pleiotropic cytokine involved in both suppressive and inflammatory immune responses in addition to a master regulator of blood vessel formation and NVU maturation (Gaengel *et al*, 2009; Winkler *et al*, 2011); and forkhead box F2 (Foxf2), a central nervous system (CNS) pericytes specific marker linked to the regulation of PC number and proliferative rate speed (Reyahi *et al*, 2015). The gene expression analysis was conducted at three different time points (Fig 2A–F): early (6 h after MIA), intermediate (E17), and long-term (P90). The early time point, i.e., 6 h after the injection of Poly I:C or vehicle into the dams, coincides with the peak of

pro-inflammatory cytokines expression into the fetal brain after the Poly I:C treatment (Corradini et al, 2018).

We found that Poly I:C male offspring show profound alterations in the expression of all the analyzed vascular-associated genes at E17, with TGF- $\beta$ 1 being the most consistently deregulated gene at all the time points (Fig 2A–C). Soon after 6 h from Poly I:C injection, male offspring already showed a reduced expression of VEGFa and a concomitant upregulation of TGF- $\beta$ 1 (Fig 2A) which persisted at P90 (Fig 2C). Conversely, gene expression analysis in the female MIA offspring revealed the alteration of a few vascular markers only at the earliest time point (GD9 + 6 h) (Fig 2D), with no apparent consequences on the subsequent maturation stages (Fig 2E and F).

Specifically, Poly I:C female offspring showed an upregulation of CD248 and TGF- $\beta$ 2 genes with a contemporary downregulation of VEGFa (Fig 2D).

We then analyzed the pattern of inflammatory cytokines response upon MIA at the same time points. In accordance with our previous study (Corradini et al, 2018), we found an elevation of IL-1 $\beta$  at early time points, which interestingly occurred specifically in males (Fig 2G). No alterations of IL-1 family members or IL-6 mRNA were detected in either males (Fig 2H and I) or females (Fig 2J–L) at any of the subsequent temporal windows. These data indicate that males and females react differently at the transcriptional level to prenatal inflammatory challenges.

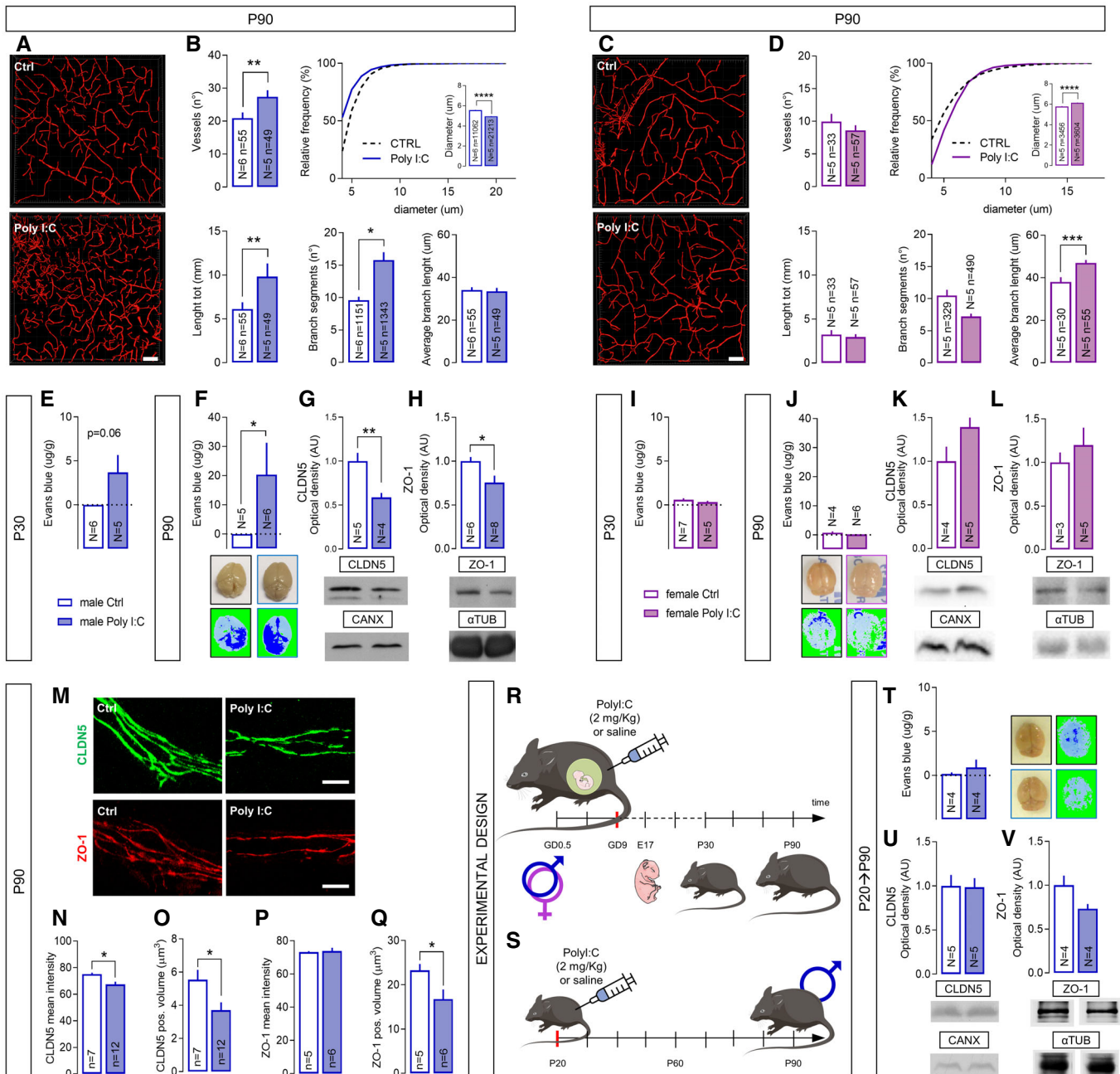


Figure 1.

**Figure 1. GD9 Poly I:C-induced MIA causes sex-specific remodeling of the brain vessels and BBB breakdown.**

- A 3D rendering of the cerebrovascular tree in brain slices from male P90 Ctrl and Poly I:C MIA offspring stained with intravascular Dil (red). Scale bar = 50  $\mu$ m.
- B Dil-positive blood vessel geometry analysis—quantification of blood vessel number, diameter (mean and cumulative frequency distribution), length, number of branch segments, and average branch length—of P90 male Ctrl and Poly I:C MIA offspring. Vessel number for Ctrl (20.93  $\pm$  1.73) and Poly I:C (27.41  $\pm$  1.99) MIA offspring, Mann–Whitney *U*-test, \*\**P* < 0.01. Mean diameter for Ctrl (5.58  $\pm$  0.01) and Poly I:C (4.96  $\pm$  0.01) MIA offspring, Mann–Whitney *U*-test, \*\*\*\**P* < 0.0001. The total length of vessel per image for Ctrl (6.12  $\pm$  0.76) and Poly I:C (9.83  $\pm$  1.48) MIA offspring, Mann–Whitney *U*-test, \*\**P* < 0.01. A number of branches for Ctrl (9.60  $\pm$  0.54) and Poly I:C (15.80  $\pm$  1.21) MIA offspring, Mann–Whitney *U*-test, \**P* < 0.05. Average branch length for Ctrl (34.07  $\pm$  1.35) and Poly I:C (33.47  $\pm$  1.67) MIA offspring.
- C 3D rendering of the cerebrovascular tree in brain slices from female P90 Ctrl and Poly I:C MIA offspring stained with intravascular Dil (red). Scale bar = 50  $\mu$ m.
- D Dil-positive blood vessel geometry analysis—quantification of blood vessel number, diameter (mean and cumulative frequency distribution), length, number of branch segments, and average branch length—of P90 female Ctrl and Poly I:C MIA offspring. Vessel number for Ctrl (9.97  $\pm$  1.18) and Poly I:C (8.61  $\pm$  0.78) MIA offspring. Mean diameter for Ctrl (5.77  $\pm$  0.03) and Poly I:C (6.16  $\pm$  0.02) MIA offspring, Mann–Whitney *U*-test, \*\*\*\**P* < 0.0001. The total length of vessel per image for Ctrl (3.23  $\pm$  0.50) and Poly I:C (2.97  $\pm$  0.30) MIA offspring. Number of branches for Ctrl (10.50  $\pm$  0.87) and Poly I:C (7.24  $\pm$  0.44) MIA offspring. Average branch length for Ctrl (38.06  $\pm$  2.17) and Poly I:C (46.93  $\pm$  1.49) MIA offspring, Mann–Whitney *U*-test, \*\*\*\**P* < 0.001.
- E Quantification of *in vivo* brain permeability at P30 in male Ctrl (0.00  $\pm$  0.00) and Poly I:C (3.68  $\pm$  1.98)-treated offspring, Mann–Whitney *U*-test, *P* = 0.060.
- F Quantification of Evans blue (EB) analysis of *in vivo* brain permeability at P90 (top) and representative pictures (bottom) of perfused brains from male Ctrl (left; 0.00  $\pm$  0.00) and Poly I:C (right; 20.32  $\pm$  10.95) offspring. Mann–Whitney *U*-test, \**P* < 0.05. In accompanying pseudocolor images, blue pixels are represented as a gradient of light-to-dark blue depending on the intensity of the color in the original photo while the absence of blue tones is represented as green.
- G Quantitative analysis of the optical density of claudin-5 (CLDN5) immunoreactive bands normalized to calnexin (CANX) in cortices from P90 male Ctrl (0.99  $\pm$  0.09) and Poly I:C (0.58  $\pm$  0.05) offspring. Mann–Whitney *U*-test, \*\**P* < 0.01.
- H Quantitative analysis of the optical density of ZO-1 immunoreactive bands normalized by  $\alpha$ -Tubulin ( $\alpha$ TUB) in cortices from P90 male Ctrl (1.00  $\pm$  0.04) and Poly I:C (0.75  $\pm$  0.08) offspring. Student's *t*-test, \**P* < 0.05.
- I Quantification of *in vivo* brain permeability at P30 in female Ctrl (0.58  $\pm$  0.17) and Poly I:C (0.31  $\pm$  0.14)-treated offspring.
- J Quantification of Evans blue (EB) analysis of *in vivo* brain permeability at P90 (top) and representative pictures (bottom) of perfused brains from female Ctrl (left; 0.70  $\pm$  0.47) and Poly I:C (right; 0.10  $\pm$  0.10) offspring. In accompanying pseudocolor images, blue pixels are represented as a gradient of light-to-dark blue depending on the intensity of the color in the original photo while the absence of blue tones is represented as green.
- K Quantitative analysis of the optical density of claudin-5 (CLDN5) immunoreactive bands normalized by CANX in cortices from P90 female Ctrl (1.00  $\pm$  0.16) and Poly I:C (1.39  $\pm$  0.13) offspring.
- L Quantitative analysis of the optical density of ZO-1 immunoreactive bands normalized by  $\alpha$ TUB in cortices from P90 female Ctrl (1.00  $\pm$  0.11) and Poly I:C (1.19  $\pm$  0.19) offspring.
- M Representative images of P90 Ctrl and Poly I:C male offspring cortices stained for TJs proteins. Claudin-5 (top green) and ZO-1 (bottom red)—scale bar = 10  $\mu$ m.
- N Quantitative analysis of the mean intensity of CLDN5 in cortices from P90 male Ctrl (75.14  $\pm$  1.08) and Poly I:C (67.39  $\pm$  2.00) offspring. Student's *t*-test, \**P* < 0.05.
- O Quantitative analysis of the CLDN5 signal volume in cortices from P90 male Ctrl (5.54  $\pm$  0.59) and Poly I:C (3.70  $\pm$  0.48) offspring. Student's *t*-test, \**P* < 0.05.
- P Quantitative analysis of the mean intensity of ZO-1 in cortices from P90 male Ctrl (73.16  $\pm$  0.59) and Poly I:C (73.86  $\pm$  1.94) offspring.
- Q Quantitative analysis of the ZO-1 signal volume in cortices from P90 male Ctrl (23.29  $\pm$  1.42) and Poly I:C (16.78  $\pm$  2.18) offspring. Student's *t*-test, \**P* < 0.05.
- R Graphical representation of MIA experimental design. Pregnant mice at GD9 were exposed to vehicle (Ctrl) or Poly I:C and the progeny, separated by sex, were analyzed at different time points (i.e., E17, P30, and P90). The figures were adapted and modified from Servier Medical Art (<http://smart.servier.com/>).
- S Graphical representation of adult immune-challenge experimental design. P20 male mice were exposed to vehicle (Ctrl) or Poly I:C to be analyzed at P90. The figures were adapted and modified from Servier Medical Art (<http://smart.servier.com/>).
- T [Left] Quantification of *in vivo* cerebrovascular permeability to EB of P90 Ctrl (0.16  $\pm$  0.16) and Poly I:C-treated (0.89  $\pm$  0.89) males injected at P20. [Right] Representative pictures of saline-perfused brains 24 h after the EB injection accompanied by pseudocolor images—blue pixels are represented as a gradient of light-to-dark blue depending on the intensity of the color in the original photo while the absence of blue tones is represented as green—from Ctrl (top) and Poly I:C (bottom) male mice.
- U Quantitative analysis of the optical density of CLDN5 immunoreactive bands normalized to CANX in cortices from P90 Ctrl (0.99  $\pm$  0.12) and Poly I:C (0.98  $\pm$  0.10) males treated at P20.
- V Quantitative analysis of the optical density of ZO-1 immunoreactive bands normalized to CANX in cortices from P90 Ctrl (1.00  $\pm$  0.11) and Poly I:C (0.73  $\pm$  0.05) males treated at P20.

Data information: Ctrl males = white bars with blue border. Poly I:C males = blue bars with blue border. Ctrl females = white bars with a purple border. Poly I:C females = purple bars with a purple border. In Fig 1B and D, black dotted lines represent the Ctrl while the blue and purple solid lines represent the male Poly I:C and female Poly I:C offspring, respectively. Numbers in bars indicate the number of animals (*N*) and images (*n*). Bars represent mean  $\pm$  SEM. Source data are available online for this figure.

To assess whether the sex-specific and temporally restricted upregulation of IL-1 $\beta$  consequent to MIA (Fig 2G) was causally linked to the observed TGF- $\beta$  pathway alteration, a gene expression analysis was performed on the cerebral tissues of IL-1R KO mice, prenatally challenged with Poly I:C or vehicle at GD9 and examined at GD9 + 6 h and E17 (Appendix Fig S3A–D). We found that, in IL-1R KO mice exposed to Poly I:C, IL-1 $\beta$  was not upregulated and no variations in TGF- $\beta$ 1-2-3 gene expression occurred, in either sex or at any developmental stages analyzed (Appendix Fig S3A–D). These data suggest a causal role of IL-1 $\beta$  in TGF- $\beta$  elevations. Further, the gender-biased response to MIA did not result from different basal levels of IL-1 gene expression, as demonstrated by the lack of sex differences in Il1 $\alpha$ , Il1 $\beta$ , and Il1rn expression levels

(Appendix Fig S3E) or IL-1 $\beta$  (Appendix Fig S3F) and IL-1ra (Appendix Fig S3G) measured by ELISA on embryo tissues.

To define whether the TGF- $\beta$  mRNA elevation occurring in the male offspring upon MIA was paralleled by protein increase in concentration, we performed TGF- $\beta$ 1 ELISA quantitation on brain tissues at E17 differentiating the latent and the biologically active form of TGF- $\beta$ 1. Interestingly, the active form of TGF- $\beta$ 1—bioavailable and capable of binding its receptor and thus exerting biological functions (Robertson & Rifkin, 2016)—was significantly increased in males (Fig 2N) but not in females (Fig 2P), while total TGF- $\beta$ 1 was not altered in males (Fig 2M) and was slightly reduced in females (Fig 2O). Of note, no elevation in TGF- $\beta$ 1 protein, neither in the active nor in the latent form, was found in the

amniotic fluid of E17 Poly I:C male mice (Appendix Fig S3H and I). These data suggest the occurrence of a brain-specific phenomenon, rather than a systemic one or maternal transfer of the inflammatory cytokine.

To further assess the activation of the TGF- $\beta$  pathway upon MIA, we performed western blot analyses of mothers against decapentaplegic (SMADs), key proteins in TGF- $\beta$  downstream signaling (Lebrin *et al*, 2005). Different subtypes of receptor-SMADs (R-SMADs) are phosphorylated in response to the direct signaling of specific TGF- $\beta$  receptors: SMAD1-5-8 are downstream to activin receptor-like kinase 1 (ALK1), while SMAD2-3 are downstream of ALK5 (Lebrin *et al*, 2005). Moreover, while ALK5 is ubiquitously expressed, ALK1 is predominantly expressed in endothelial cells (ECs) (Armulik *et al*, 2005; González-Núñez

*et al*, 2013). SMAD4 is the only known co-regulator of the heterotrimeric complex required for the nuclear translocation of R-SMAD (Li *et al*, 2011). Western blotting analysis of the cerebral cortex tissues of Poly I:C male offspring at E17 (Fig 2Q-S) revealed the specific upregulation of pSMAD1-5 (phospho-SMAD1-5) (Fig 2Q) in Poly I:C males compared to gender-matched controls, while no alterations were found in the levels of pSMAD2 (Fig 2R) and SMAD4 (Fig 2S). Conversely, Poly I:C females did not display variation in any of the SMADs, when compared to the gender-matched controls (Fig 2T-V), further confirming the lack of enhanced TGF- $\beta$  signaling. These data indicate a male-specific ALK1-SMAD1-5 signaling axis alteration in response to MIA, which suggests an EC-specific excessive activation of the TGF- $\beta$  signaling.

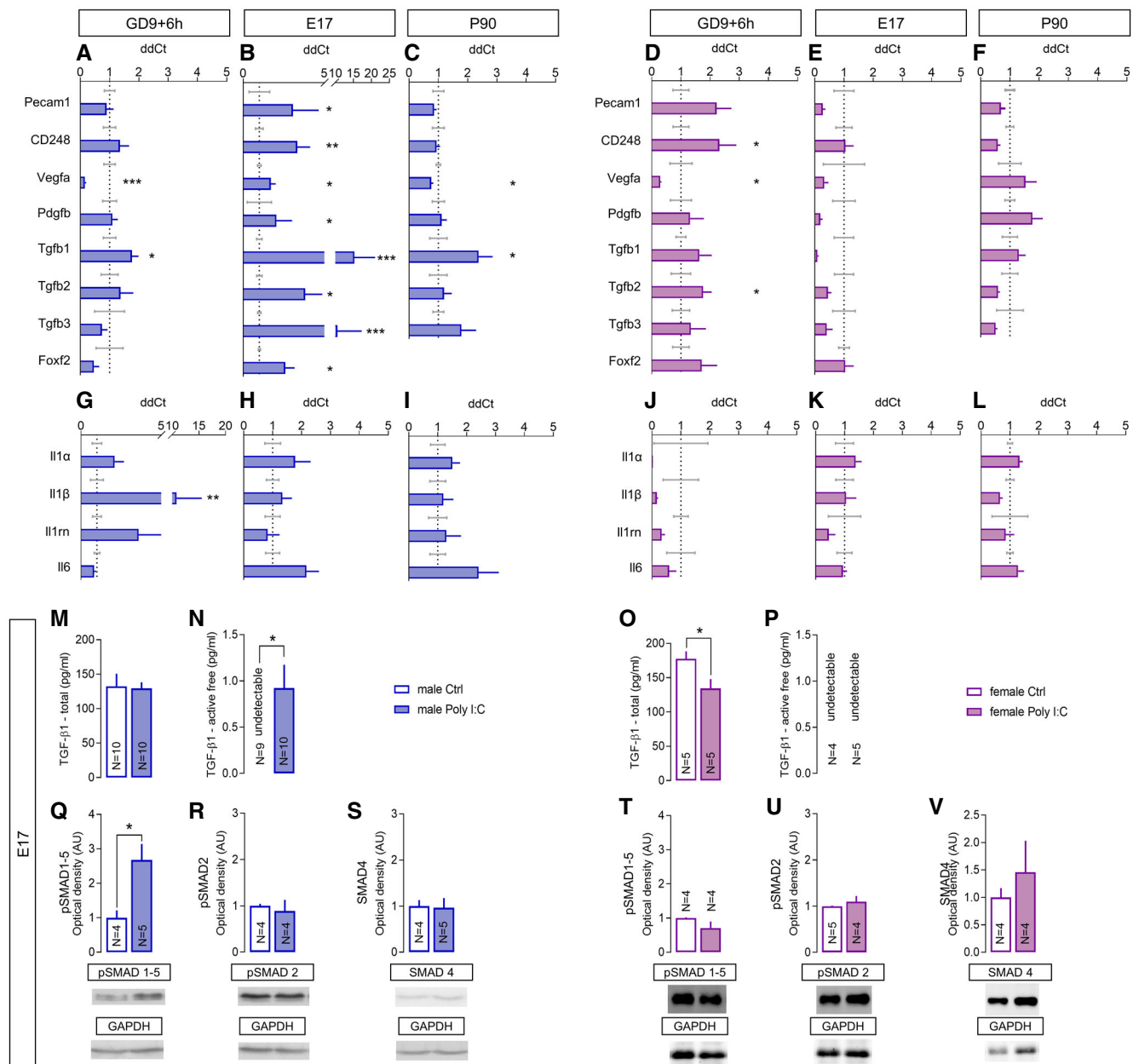


Figure 2.

**Figure 2. Maternal immune activation causes sex-specific alterations in the expression of vascular and inflammatory controller molecules.**

- A qPCR analyses of GD9 + 6 h male embryos for: *Pecam1* (Ctrl =  $1.00 \pm 0.17$  N = 8, Poly I:C =  $0.89 \pm 0.23$  N = 13), *CD248* (Ctrl =  $1.00 \pm 0.20$  N = 6, Poly I:C =  $1.35 \pm 0.31$  N = 11), *Vegfa* (Ctrl =  $1.00 \pm 0.19$  N = 8, Poly I:C =  $0.15 \pm 0.04$  N = 8, Student's *t*-test,  $***P < 0.001$ ), *Pdfrb* (Ctrl =  $1.00 \pm 0.23$  N = 5, Poly I:C =  $1.10 \pm 0.18$  N = 13), *Tgfb1* (Ctrl =  $1.00 \pm 0.21$  N = 7, Poly I:C =  $1.76 \pm 0.22$  N = 10, Mann-Whitney *U*-test,  $*P < 0.05$ ), *Tgfb2* (Ctrl =  $1.00 \pm 0.28$  N = 6, Poly I:C =  $1.37 \pm 0.28$  N = 13), *Tgfb3* (Ctrl =  $1.00 \pm 0.51$  N = 6, Poly I:C =  $0.73 \pm 0.19$  N = 10), and *Foxf2* (Ctrl =  $1.00 \pm 0.45$  N = 8, Poly I:C =  $0.46 \pm 0.18$  N = 13) mRNAs.
- B qPCR analyses of E17 male cortices for: *Pecam1* (Ctrl =  $1.00 \pm 0.63$  N = 10, Poly I:C =  $3.07 \pm 1.58$  N = 8; Mann-Whitney *U*-test,  $*P < 0.05$ ), *CD248* (Ctrl =  $1.00 \pm 0.23$  N = 10, Poly I:C =  $3.33 \pm 0.79$  N = 9; Mann-Whitney *U*-test,  $**P < 0.01$ ), *Vegfa* (Ctrl =  $1.00 \pm 0.10$  N = 8, Poly I:C =  $1.70 \pm 0.29$  N = 5; Mann-Whitney *U*-test,  $*P < 0.05$ ), *Pdfrb* (Ctrl =  $1.00 \pm 0.75$  N = 9, Poly I:C =  $2.05 \pm 0.96$  N = 9; Mann-Whitney *U*-test,  $*P < 0.05$ ), *Tgfb1* (Ctrl =  $1.00 \pm 0.16$  N = 7, Poly I:C =  $15.27 \pm 5.75$  N = 7; Mann-Whitney *U*-test,  $***P < 0.001$ ), *Tgfb2* (Ctrl =  $1.00 \pm 0.16$  N = 8, Poly I:C =  $3.82 \pm 1.05$  N = 6; Mann-Whitney *U*-test,  $*P < 0.05$ ), *Tgfb3* (Ctrl =  $1.00 \pm 0.10$  N = 9, Poly I:C =  $10.58 \pm 6.73$  N = 8; Mann-Whitney *U*-test,  $***P < 0.001$ ); and *Foxf2* (Ctrl =  $1.00 \pm 0.06$  N = 5, Poly I:C =  $2.60 \pm 0.57$  N = 8; Mann-Whitney *U*-test,  $*P < 0.05$ ) mRNAs.
- C qPCR analyses of P90 male cortices for: *Pecam1* (Ctrl =  $1.00 \pm 0.18$  N = 8, Poly I:C =  $0.85 \pm 0.08$  N = 8), *CD248* (Ctrl =  $1.00 \pm 0.20$  N = 9, Poly I:C =  $0.93 \pm 0.11$  N = 8), *Vegfa* (Ctrl =  $1.00 \pm 0.07$  N = 8, Poly I:C =  $0.75 \pm 0.06$  N = 8; Mann-Whitney *U*-test,  $*P < 0.05$ ); *Pdfrb* (Ctrl =  $1.00 \pm 0.20$  N = 8, Poly I:C =  $1.11 \pm 0.17$  N = 4), *Tgfb1* (Ctrl =  $1.00 \pm 0.29$  N = 5, Poly I:C =  $2.37 \pm 0.47$  N = 7; Mann-Whitney *U*-test,  $*P < 0.05$ ); *Tgfb2* (Ctrl =  $1.00 \pm 0.29$  N = 4, Poly I:C =  $1.19 \pm 0.26$  N = 7), and *Tgfb3* (Ctrl =  $1.00 \pm 0.18$  N = 10, Poly I:C =  $1.78 \pm 0.50$  N = 11) mRNAs.
- D qPCR analyses of GD9 + 6 h female embryos for: *Pecam1* (Ctrl =  $1.00 \pm 0.27$  N = 10, Poly I:C =  $2.22 \pm 0.50$  N = 6), *CD248* (Ctrl =  $1.00 \pm 0.27$  N = 10, Poly I:C =  $2.32 \pm 0.57$  N = 6; Mann-Whitney *U*-test,  $*P < 0.05$ ), *Vegfa* (Ctrl =  $1.00 \pm 0.38$  N = 8, Poly I:C =  $0.29 \pm 0.03$  N = 5; Mann-Whitney *U*-test,  $*P < 0.05$ ), *Pdfrb* (Ctrl =  $1.00 \pm 0.36$  N = 10, Poly I:C =  $1.31 \pm 0.47$  N = 6), *Tgfb1* (Ctrl =  $1.00 \pm 0.16$  N = 8, Poly I:C =  $1.63 \pm 0.42$  N = 7), *Tgfb2* (Ctrl =  $1.00 \pm 0.33$  N = 9, Poly I:C =  $1.75 \pm 0.29$  N = 6; Mann-Whitney *U*-test,  $*P < 0.05$ ), *Tgfb3* (Ctrl =  $1.00 \pm 0.29$  N = 9, Poly I:C =  $1.33 \pm 0.51$  N = 6), and *Foxf2* (Ctrl =  $1.00 \pm 0.28$  N = 9, Poly I:C =  $1.71 \pm 0.52$  N = 6) mRNAs.
- E qPCR analyses of E17 female cortices for: *Pecam1* (Ctrl =  $1.00 \pm 0.34$  N = 6, Poly I:C =  $0.27 \pm 0.08$  N = 8), *CD248* (Ctrl =  $1.00 \pm 0.27$  N = 8, Poly I:C =  $1.04 \pm 0.28$  N = 9), *Vegfa* (Ctrl =  $1.00 \pm 0.70$  N = 5, Poly I:C =  $0.32 \pm 0.13$  N = 5), *Pdfrb* (Ctrl =  $1.00 \pm 0.38$  N = 6, Poly I:C =  $0.19 \pm 0.07$  N = 9), *Tgfb1* (Ctrl =  $1.00 \pm 0.33$  N = 5, Poly I:C =  $0.09 \pm 0.03$  N = 6), *Tgfb2* (Ctrl =  $1.00 \pm 0.32$  N = 7, Poly I:C =  $0.45 \pm 0.11$  N = 8), *Tgfb3* (Ctrl =  $1.00 \pm 0.38$  N = 7, Poly I:C =  $0.40 \pm 0.20$  N = 9), and *Foxf2* (Ctrl =  $1.00 \pm 0.18$  N = 5, Poly I:C =  $1.04 \pm 0.28$  N = 8) mRNAs.
- F qPCR analyses of P90 female cortices for: *Pecam1* (Ctrl =  $1.00 \pm 0.15$  N = 5, Poly I:C =  $0.69 \pm 0.15$  N = 5), *CD248* (Ctrl =  $1.00 \pm 0.13$  N = 5, Poly I:C =  $0.58 \pm 0.09$  N = 5), *Vegfa* (Ctrl =  $1.00 \pm 0.38$  N = 6, Poly I:C =  $1.53 \pm 0.38$  N = 8), *Pdfrb* (Ctrl =  $1.00 \pm 0.16$  N = 9, Poly I:C =  $1.77 \pm 0.35$  N = 17), *Tgfb1* (Ctrl =  $1.00 \pm 0.26$  N = 13, Poly I:C =  $1.30 \pm 0.23$  N = 14), *Tgfb2* (Ctrl =  $1.00 \pm 0.27$  N = 11, Poly I:C =  $0.59 \pm 0.06$  N = 4), and *Tgfb3* (Ctrl =  $1.00 \pm 0.45$  N = 11, Poly I:C =  $0.51 \pm 0.06$  N = 4) mRNAs.
- G qPCR analyses of GD9 + 6 h male embryos for *Il1 $\alpha$*  (Ctrl =  $1.00 \pm 0.29$  N = 7, Poly I:C =  $2.10 \pm 0.57$  N = 17), *Il1 $\beta$*  (Ctrl =  $1.00 \pm 0.39$  N = 6, Poly I:C =  $10.84 \pm 4.70$  N = 6; Mann-Whitney *U*-test,  $**P < 0.01$ ), *Il1rn* (Ctrl =  $1.00 \pm 0.27$  N = 7, Poly I:C =  $3.60 \pm 1.58$  N = 11), and *Il6* (Ctrl =  $1.00 \pm 0.17$  N = 6, Poly I:C =  $0.82 \pm 0.12$  N = 7) mRNAs.
- H qPCR analyses of E17 male cortices for: *Il1 $\alpha$*  (Ctrl =  $1.00 \pm 0.27$  N = 9, Poly I:C =  $1.77 \pm 0.53$  N = 11), *Il1 $\beta$*  (Ctrl =  $1.00 \pm 0.21$  N = 7, Poly I:C =  $1.33 \pm 0.33$  N = 8), *Il1rn* (Ctrl =  $1.00 \pm 0.25$  N = 10, Poly I:C =  $0.82 \pm 0.40$  N = 18), and *Il6* (Ctrl =  $1.00 \pm 0.24$  N = 7, Poly I:C =  $2.17 \pm 0.43$  N = 8) mRNAs.
- I qPCR analyses of P90 male cortices for: *Il1 $\alpha$*  (Ctrl =  $1.00 \pm 0.24$  N = 8, Poly I:C =  $1.51 \pm 0.26$  N = 10), *Il1 $\beta$*  (Ctrl =  $1.00 \pm 0.27$  N = 8, Poly I:C =  $1.19 \pm 0.34$  N = 8), *Il1rn* (Ctrl =  $1.00 \pm 0.31$  N = 18, Poly I:C =  $1.30 \pm 0.50$  N = 14), and *Il6* (Ctrl =  $1.00 \pm 0.27$  N = 7, Poly I:C =  $2.40 \pm 0.70$  N = 8) mRNAs.
- J qPCR analyses of GD9 + 6 h female embryos for: *Il1 $\alpha$*  (Ctrl =  $1.00 \pm 0.93$  N = 6, Poly I:C =  $0.03 \pm 0.00$  N = 4), *Il1 $\beta$*  (Ctrl =  $1.00 \pm 0.61$  N = 5, Poly I:C =  $0.17 \pm 0.04$  N = 7), *Il1rn* (Ctrl =  $1.00 \pm 0.25$  N = 9, Poly I:C =  $0.33 \pm 0.11$  N = 7), and *Il6* (Ctrl =  $1.00 \pm 0.48$  N = 7, Poly I:C =  $0.59 \pm 0.24$  N = 5) mRNAs.
- K qPCR analyses of E17 female cortices for: *Il1 $\alpha$*  (Ctrl =  $1.00 \pm 0.31$  N = 5, Poly I:C =  $1.38 \pm 0.20$  N = 12), *Il1 $\beta$*  (Ctrl =  $1.00 \pm 0.30$  N = 5, Poly I:C =  $1.05 \pm 0.35$  N = 7), *Il1rn* (Ctrl =  $1.00 \pm 0.55$  N = 6, Poly I:C =  $0.45 \pm 0.22$  N = 6), and *Il6* (Ctrl =  $1.00 \pm 0.26$  N = 7, Poly I:C =  $0.94 \pm 0.14$  N = 8) mRNAs.
- L qPCR analyses of P90 female cortices for *Il1 $\alpha$*  (Ctrl =  $1.00 \pm 0.08$  N = 5, Poly I:C =  $1.32 \pm 0.11$  N = 9), *Il1 $\beta$*  (Ctrl =  $1.00 \pm 0.13$  N = 5, Poly I:C =  $0.65 \pm 0.09$  N = 8), *Il1rn* (Ctrl =  $1.00 \pm 0.61$  N = 4, Poly I:C =  $0.85 \pm 0.29$  N = 7), and *Il6* (Ctrl =  $1.00 \pm 0.11$  N = 9, Poly I:C =  $1.28 \pm 0.20$  N = 20) mRNAs. Values are normalized over control (dashed line).
- M ELISA quantification of total TGF- $\beta$ 1 in E17 male embryos brains as pg/ml (Ctrl =  $132.6 \pm 18.14$  and Poly I:C =  $129.6 \pm 8.62$ ).
- N ELISA quantification of active free TGF- $\beta$ 1 in E17 male embryos brains as pg/ml (Ctrl = undetectable and Poly I:C =  $0.92 \pm 0.25$ ).
- O ELISA quantification of total TGF- $\beta$ 1 in E17 female embryos brains as pg/ml (Ctrl =  $177.6 \pm 10.88$  and Poly I:C =  $134.4 \pm 13.59$ ).
- P ELISA quantification of active free TGF- $\beta$ 1 in E17 female embryos brains as pg/ml (undetectable).
- Q-S Western Blotting quantification of SMAD proteins in E17 male cortices for (Q) pSMAD1-5 (Ctrl =  $0.99 \pm 0.21$ , Poly I:C =  $2.67 \pm 0.46$ ); Mann-Whitney *U*-test,  $*P < 0.05$ , (R) pSMAD2 (Ctrl =  $1.00 \pm 0.04$ , Poly I:C =  $0.88 \pm 0.24$ ), and (S) SMAD4 (Ctrl =  $1.00 \pm 0.12$ , Poly I:C =  $0.96 \pm 0.21$ ). Protein levels were normalized to GAPDH.
- T-V Western blotting quantification of SMAD proteins in E17 female cortices for (T) pSMAD1-5 (Ctrl =  $1.00 \pm 0.02$ , Poly I:C =  $0.70 \pm 0.18$ ), (U) pSMAD2 (Ctrl =  $1.00 \pm 0.01$ , Poly I:C =  $1.09 \pm 0.12$ ), and (V) SMAD4 (Ctrl =  $1.00 \pm 0.16$ , Poly I:C =  $1.46 \pm 0.57$ ). Protein levels were normalized to GAPDH.
- Data information: Ctrl males = white bars with blue border. Poly I:C males = blue bars with blue border. Ctrl females = white bars with purple border. Poly I:C females = purple bars with purple border. Numbers in bars indicate the number of animals (N). Bars represent mean  $\pm$  SEM.
- Source data are available online for this figure.

### Vascular cells sorted from the cerebral cortex of MIA offspring form a leaky barrier *in vitro*

So far, our data indicate that male—but not female—offspring of dams treated with 2 mg/kg Poly I:C at GD9 display, as adults, increased vessel permeability and reduced expression of tight junction proteins. To define whether the MIA protocol affects the properties of the cells composing the blood vessels in a cell-autonomous manner already at an early stage, we sorted ECs and pericytes (PCs) from the cerebral cortices of E17 MIA offspring and exploited them to model *ex vivo* cell barriers formed by either ECs alone or PCs co-

cultured with bEnd.3 cells (Lauranzano *et al*, 2019). ECs and PCs identities were confirmed after sorting and cell maintenance in culture. ECs were characterized by acetylated low-density lipoprotein (Ac-LDL) uptake ability (Appendix Fig S4A), which is typical of macrophages and ECs (Via *et al*, 1985), while PCs were identified as positive for platelet-derived growth factor receptor beta (PDGFR $\beta$ ) and neural/glial antigen 2 (NG2), and negative for the neuronal marker neuronal nuclear protein (NeuN) and the astrocytic marker glial fibrillary acidic protein (GFAP) (Appendix Fig S4B). Analyses of *in vitro* barriers, formed by ECs (Fig 3A and B) or PCs + bEnd.3 cells (Fig 3C and D) from Poly I:C offspring, revealed defects

selectively in the barriers formed by male-derived cells. Indeed, the BBBs made with male-derived Poly I:C offspring's ECs displayed enhanced permeability relative to the gender-matched control (Fig 3B), and bEnd.3 cells co-cultured with male-derived Poly I:C offspring's PCs displayed a lower transendothelial electrical resistance (TEER) (Fig 3C). No difference was detected in the barriers formed by female-derived cells (Fig 3A and B). Of note, in the presence of PCs, all barriers showed a reduced permeability compared to bEND.3 cultured alone, indicating a gain in tightness upon the addition of PCs to the *in vitro* model (Fig 3D).

We next assessed whether the elevation of TGF- $\beta$  could be directly responsible for the damage to the barrier properties. To this

aim, ECs and PCs were isolated from untreated E17 males or female embryos and exploited for the construction of EC (Fig 3E) or PC + bEnd.3 (Fig 3F) barrier prototypes. Exposure of either barrier type to TGF- $\beta$  for 72 h resulted in a progressive TEER decrease (Fig 3E and F), with no overt changes in permeability (Fig 3G and H). These data indicate that: (i) TGF- $\beta$  has a deleterious effect when applied to ECs or PCs at early developmental stages, and (ii) both male and female vascular cells are sensitive to the cytokine.

A possible reason for the TGF- $\beta$  deleterious effect is the fact that TGF- $\beta$  dampens the expression of CD146 in ECs, an event that physiologically occurs during development when ECs recruit and contact PCs (Chen *et al*, 2017). CD146 is a key component of EC-PC

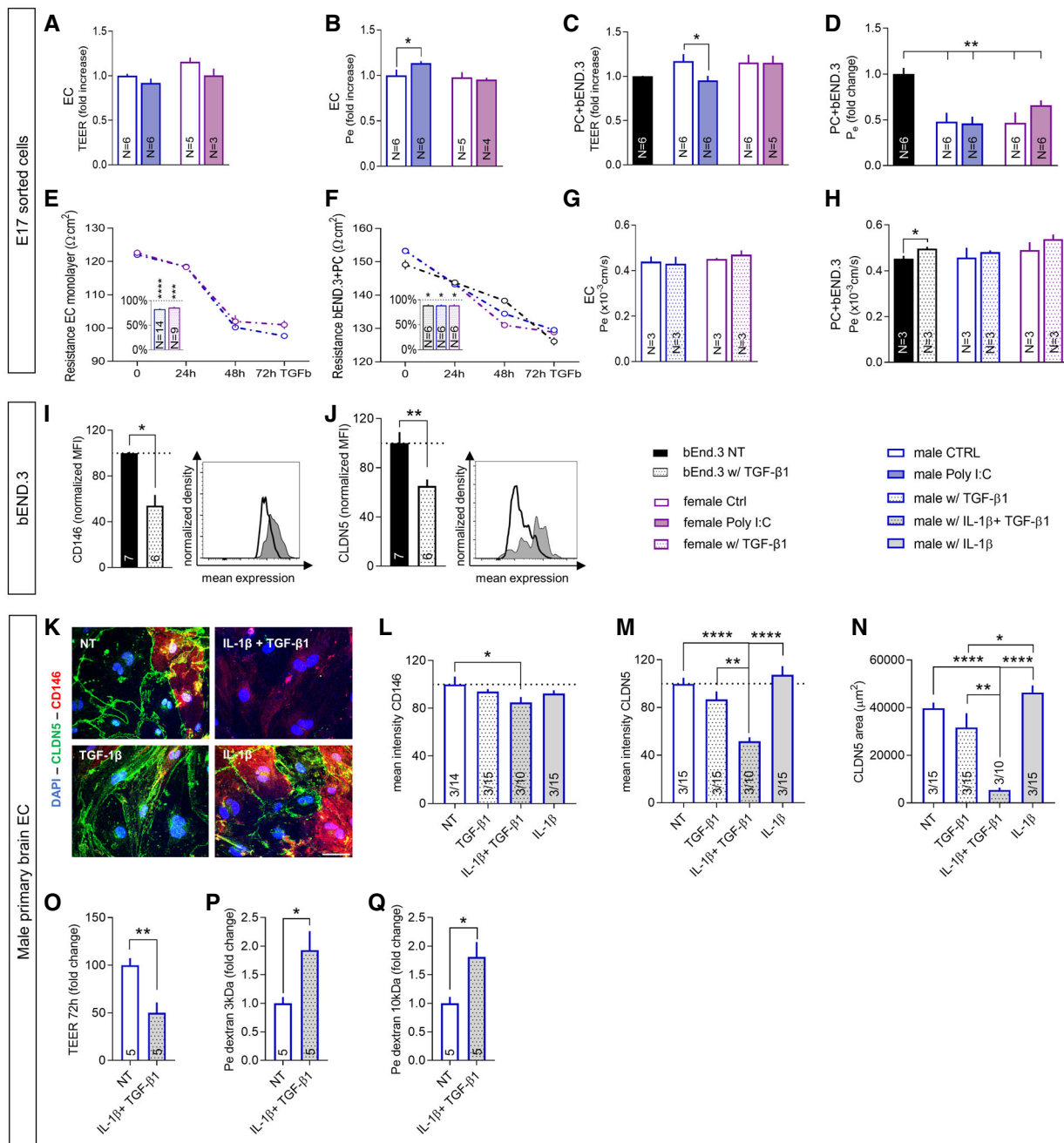


Figure 3.

**Figure 3. TGF- $\beta$ 1 dampens the expression of CD146 and claudin-5 and reduces the tightness of *in vitro* barrier models—independently of the sex.**

- A TEER of the *in vitro* BBB models composed by a monolayer of ECs sorted from E17 Male Ctrl ( $1.00 \pm 0.02$ ), male Poly I:C ( $0.92 \pm 0.04$ ), female Ctrl ( $1.15 \pm 0.04$ ), and female Poly I:C ( $1.00 \pm 0.07$ ) offspring. Data are normalized to male Ctrl.
- B Permeability to 10 kDa dextran of the *in vitro* BBB models composed by a monolayer of sorted ECs from male Ctrl ( $1.00 \pm 0.06$ ), male Poly I:C ( $1.13 \pm 0.02$ ), female Ctrl ( $0.97 \pm 0.05$ ), and female Poly I:C ( $0.95 \pm 0.01$ ) offspring. Mann–Whitney *U*-test,  $*P < 0.05$ . Data are normalized to male Ctrl.
- C TEER of barriers composed of bEND.3 alone ( $1.00 \pm 0.00$ ) or co-cultured with sorted PCs from male Ctrl ( $1.17 \pm 0.07$ ), male Poly I:C ( $0.95 \pm 0.05$ ), female Ctrl ( $1.15 \pm 0.08$ ), and female Poly I:C ( $1.15 \pm 0.08$ ) offspring. Mann–Whitney *U*-test,  $*P < 0.05$ . Data are normalized to bEnd.3.
- D Permeability to 10 kDa dextran of barriers composed by a monolayer of bEND.3 alone ( $1.00 \pm 0.06$ ) or co-cultured with sorted PCs from male Ctrl ( $0.47 \pm 0.09$ ), male Poly I:C ( $0.46 \pm 0.07$ ), female Ctrl ( $0.46 \pm 0.11$ ), and female Poly I:C ( $0.65 \pm 0.05$ ) offspring. One sample *t*-test,  $**P < 0.01$ . Data are normalized to bEnd.3.
- E TEER ( $\Omega \cdot \text{cm}^2$ ) was monitored over 72 h treatment with TGF- $\beta$ 1 and normalized to baseline in BBB models composed by a monolayer of sorted ECs from male (72 h TGF- $\beta$ 1 =  $82.85 \pm 1.56$ ) or female (72 h TGF- $\beta$ 1 =  $85.92 \pm 2.03$ ) embryos. The insert shows the values at 72 h (bars) normalized to the 0 h values (dashed line). One sample *t*-test,  $***P < 0.001$  and  $****P < 0.0001$ .
- F TEER ( $\Omega \cdot \text{cm}^2$ ) was monitored over 72 h treatment with TGF- $\beta$ 1 and normalized to baseline in barrier models composed by a monolayer of bEND.3 alone (72 h TGF- $\beta$ 1 =  $89.85 \pm 2.05$ ) or co-cultured with sorted PCs from male (72 h TGF- $\beta$ 1 =  $88.83 \pm 1.93$ ) or female (72 h TGF- $\beta$ 1 =  $89.02 \pm 2.22$ ) embryos. The insert shows the values at 72 h (bars) normalized to the 0 h values (dashed line). Wilcoxon signed-rank test,  $*P < 0.05$ .
- G 10 kDa dextran permeability after 72 h TGF- $\beta$ 1 treatment of the *in vitro* BBBs prototypes composed by a monolayer made of sorted ECs from male NT ( $0.43 \pm 0.02$ ), male TGF- $\beta$ 1 ( $0.43 \pm 0.03$ ); female NT ( $0.45 \pm 0.00$ ), and female TGF- $\beta$ 1 ( $0.47 \pm 0.01$ ).
- H 10 kDa dextran permeability 72 h after TGF- $\beta$ 1 treatment of NVU prototypes composed by a monolayer made of bEND.3 alone (NT, solid black bar =  $0.45 \pm 0.01$ ; TGF- $\beta$ 1, dotted black bar =  $0.49 \pm 0.00$ ) and co-cultured with sorted PCs from male (NT =  $0.45 \pm 0.04$ , TGF- $\beta$ 1 =  $0.48 \pm 0.00$ ) or female (NT =  $0.49 \pm 0.03$ , TGF- $\beta$ 1 =  $0.53 \pm 0.02$ ) embryos. Student's *t*-test,  $*P < 0.05$ .
- I FACS quantitative data of the normalized MFI of CD146 (NT =  $100.00 \pm 1.14$ , TGF- $\beta$ 1 =  $54.08 \pm 9.42$ ; Student's *t*-test,  $*P < 0.05$ ) and representative histogram of untreated (solid gray) and TGF- $\beta$ 1-treated cells (hollow black bold line).
- J FACS quantitative data of the normalized MFI of claudin-5 (CLDN5; NT =  $100.00 \pm 8.94$ , TGF- $\beta$ 1 =  $65.22 \pm 5.29$ ; Student's *t*-test,  $**P < 0.01$ ) and representative histogram of untreated (solid gray) and TGF- $\beta$ 1-treated cells (hollow black bold line).
- K Representative images of monolayers of primary endothelial cells isolated from male brains and stained for CD146 (red) and CLDN5 (green) under control conditions (NT) or upon treatment with different cytokines. Scale bar = 50  $\mu\text{m}$ .
- L Quantitative analysis of CD146 immunofluorescence mean intensity measured in primary male brain EC monolayers under control conditions or after 72 h treatments with different cytokines: NT =  $100.00 \pm 6.55$ , TGF- $\beta$ 1 =  $94.03 \pm 2.01$ , IL-1 $\beta$  + TGF- $\beta$ 1 =  $84.87 \pm 4.59$ , and IL-1 $\beta$  =  $92.34 \pm 2.65$ ; Kruskal–Wallis,  $*P < 0.05$ .
- M Quantitative analysis of claudin-5 immunofluorescence mean intensity in primary male brain EC monolayers under control conditions or after 72 h treatments with different cytokines: NT =  $99.76 \pm 5.19$ , TGF- $\beta$ 1 =  $86.74 \pm 6.76$ , IL-1 $\beta$  + TGF- $\beta$ 1 =  $51.64 \pm 3.31$ , and IL-1 $\beta$  =  $107.3 \pm 7.37$ ; ordinary one-way ANOVA,  $**P < 0.01$ ,  $****P < 0.0001$ .
- N Quantitative analysis of claudin-5 immunofluorescence area ( $\mu\text{m}^2$ ) in primary male brain EC monolayers under control conditions or after 72 h treatments with different cytokines: NT =  $39,781 \pm 2,342$ , TGF- $\beta$ 1 =  $31,707 \pm 5,939$ , IL-1 $\beta$  + TGF- $\beta$ 1 =  $5,415 \pm 1,037$ , and IL-1 $\beta$  =  $46,303 \pm 2,986$ ; ordinary one-way ANOVA,  $*P < 0.05$ ,  $**P < 0.01$ ,  $****P < 0.0001$ .
- O Graph showing TEER measured by volt ohmmeter at 72 h normalized in NT ( $100.00 \pm 7.46$ ) and IL-1 $\beta$  + TGF- $\beta$ 1 ( $49.93 \pm 10.96$ )-treated primary male brain EC cultures. Student's *t*-test,  $**P < 0.01$ . Data are normalized to  $t_0$ .
- P Permeability to 3 kDa dextran quantified by fluorescence spectrophotometry in NT ( $1.00 \pm 0.10$ ) and IL-1 $\beta$  + TGF- $\beta$ 1 ( $1.92 \pm 0.33$ )-treated primary male brain EC cultures. Student's *t*-test,  $*P < 0.05$ .
- Q Permeability to 10 kDa dextran quantified by fluorescence spectrophotometry in NT ( $1.00 \pm 0.11$ ) and IL-1 $\beta$  + TGF- $\beta$ 1 ( $1.80 \pm 0.26$ )-treated primary male brain EC cultures. Student's *t*-test,  $*P < 0.05$ .

Data information: A–H. Embryos prenatally exposed to vehicle (Ctrl) or Poly I:C on GD9 were dissected, and cortex-derived vascular cells were used to build *in vitro* barrier models. K–Q. Cortex-derived ECs isolated from male mice at 2 months were used to build *in vitro* barrier models and analyzed. bEnd.3 cells = bars with black border. Cells derived from Ctrl males = white bars with blue border. Cells derived from Poly I:C males = blue bars with blue border. Cells derived from Ctrl females = white bars with purple border. Cells derived from Poly I:C females = purple bars with purple border. In Fig 3E and F, blue and purple dotted lines represent cells derived from male and female brains, respectively. The black dotted line represents bEnd.3 cultures. Numbers in bars indicate the number of animals (*N*) or independent cultures/pictures. Bars represent mean  $\pm$  SEM.

Source data are available online for this figure.

signaling and its absence, as in the case of CD146 KO mice, results in uncoordinated pericyte recruitment, reduction in EC claudin-5 expression, and altered blood vessel pericyte coverage (Chen *et al*, 2017). Accordingly, exposure of bEnd.3 cells to TGF- $\beta$ 1 led to a decrease in the expression of both CD146 (Fig 3I) and claudin-5 (Fig 3J). Thus, to fully mimic the cytokine storm that occurs in the MIA model (see Fig 2) and assess if the interaction of the two main cytokines involved (i.e., IL-1 $\beta$  and TGF- $\beta$ 1) synergically impacts the brain ECs, male-derived primary endothelial cells were maintained in culture until the formation of a mature, confluent monolayer (Appendix Fig S4C). Under these conditions, the immunocytochemical staining for claudin-5 revealed a distribution at the cell-to-cell interface, which represents the typical pattern of a fully mature BBB. Endothelial cell monolayers were then challenged with TGF- $\beta$ 1, IL-1 $\beta$ , or with a combination of the two cytokines and stained for CD146 and claudin-5 (Fig 3K). CD146 expression was

significantly reduced only by the synergic effect of IL-1 $\beta$  and TGF- $\beta$ 1 (Fig 3L). Coherently, claudin-5 mean intensity (Fig 3M) and claudin-5-positive area (Fig 3N), although slightly reduced by the treatment with TGF- $\beta$  alone, were significantly dampened only by the concomitant treatment with IL-1 $\beta$  and TGF- $\beta$ 1 (Fig 3M and N). Similar results were obtained in monolayers of endothelial cells isolated from female cortices (Appendix Fig S4D–F). Finally, we further evaluated the response of primary endothelial cells to the treatment with a combination of IL-1 $\beta$  and TGF- $\beta$ 1 by measuring TEER and permeability to different sizes of dextran molecules, two strong indicators of the integrity of the cellular barriers. The results indicated a significant reduction in the TEER in monolayers formed by male (Fig 3O) or female EC (Appendix Fig S4G) and increased permeability to both 3 kDa (Fig 3P) and 10 kDa (Fig 3Q) dextran. Besides demonstrating the deleterious effect of TGF- $\beta$ 1 and IL-1 $\beta$  on brain vascular cells, these data indicate that cells from males and



females are equally susceptible to the cytokine application. Therefore, the barrier defects occurring specifically in males are imputable to the male-specific cytokine elevation upon Poly I:C exposure at GD9.

**Prenatally exposed poly I:C males display anomalies in the cerebrovascular organization of endothelial cells and pericytes**

To then assess whether ECs and PCs display molecular derangements upon MIA, ECs and PCs from male or female cortical blood vessels were isolated and analyzed by FACS at two time points: E17, when angiogenesis is intensely active, and P30, when the angiogenesis process is mostly ended (Coelho-Santos & Shih, 2020). ECs were identified and accordingly gated, as CD45<sup>-</sup>CD31<sup>+</sup> cells, while PCs were identified as CD45<sup>-</sup>CD146<sup>+</sup> at E17 (Fig 4A) and as CD45<sup>-</sup>CD146<sup>+</sup>CD13<sup>+</sup> at P30 (Fig 4C). We first analyzed the relative amount of the two cell types in control and Poly I:C offspring, in a sex-dependent manner. At E17, Poly I:C male offspring, but not female, displayed an EC/PC ratio higher than the respective control (Fig 4B). This dysregulation was time restricted, as it was undetectable at P30 (Fig 4D). To investigate the origin of the EC/PC altered ratio, we examined the proliferation rate of these cells by

EdU (Fig 4E–J), a fluorescent cell-permeable uridine synthetic nucleoside which integrates into the DNA of proliferative cells during replication. EdU was injected at GD17 (5 h before sacrifice) in pregnant mice treated at GD9 with either Poly I:C or vehicle and in P30 Poly I:C offspring (48 h before sacrifice) (Appendix Fig S5A). Results indicated that E17 Poly I:C male offspring display a reduction in the cell proliferative rate compared to control males (Fig 4E), a difference which persisted at P30 (Fig 4H). FACS analysis of ECs and PCs showed a significant and specific reduction in PC proliferation at both E17 and P30 (Fig 4F and I) in the absence of proliferative alterations of ECs (Fig 4G and J). Furthermore, in the control setting, we confirmed the occurrence of a lower proliferative rate of brain cells in E17 females (Fig 4E), which disappeared at P30 (Fig 4H) as already described (Bowers et al, 2010).

We then quantified in ECs and PCs the expression of CD146 (Chen et al, 2017) and CD105, a type I transmembrane protein, known to induce endothelial cell activation and proliferation by serving as an auxiliary receptor for TGF-β. A consistent reduction in CD146 expression was detected in ECs of Poly I:C male offspring relative to control at both P30 (Fig 4K) and E17 (Appendix Fig S5B). This was paralleled by a higher CD146 mean fluorescence intensity (MFI) in cerebral ECs of control males relative to control females

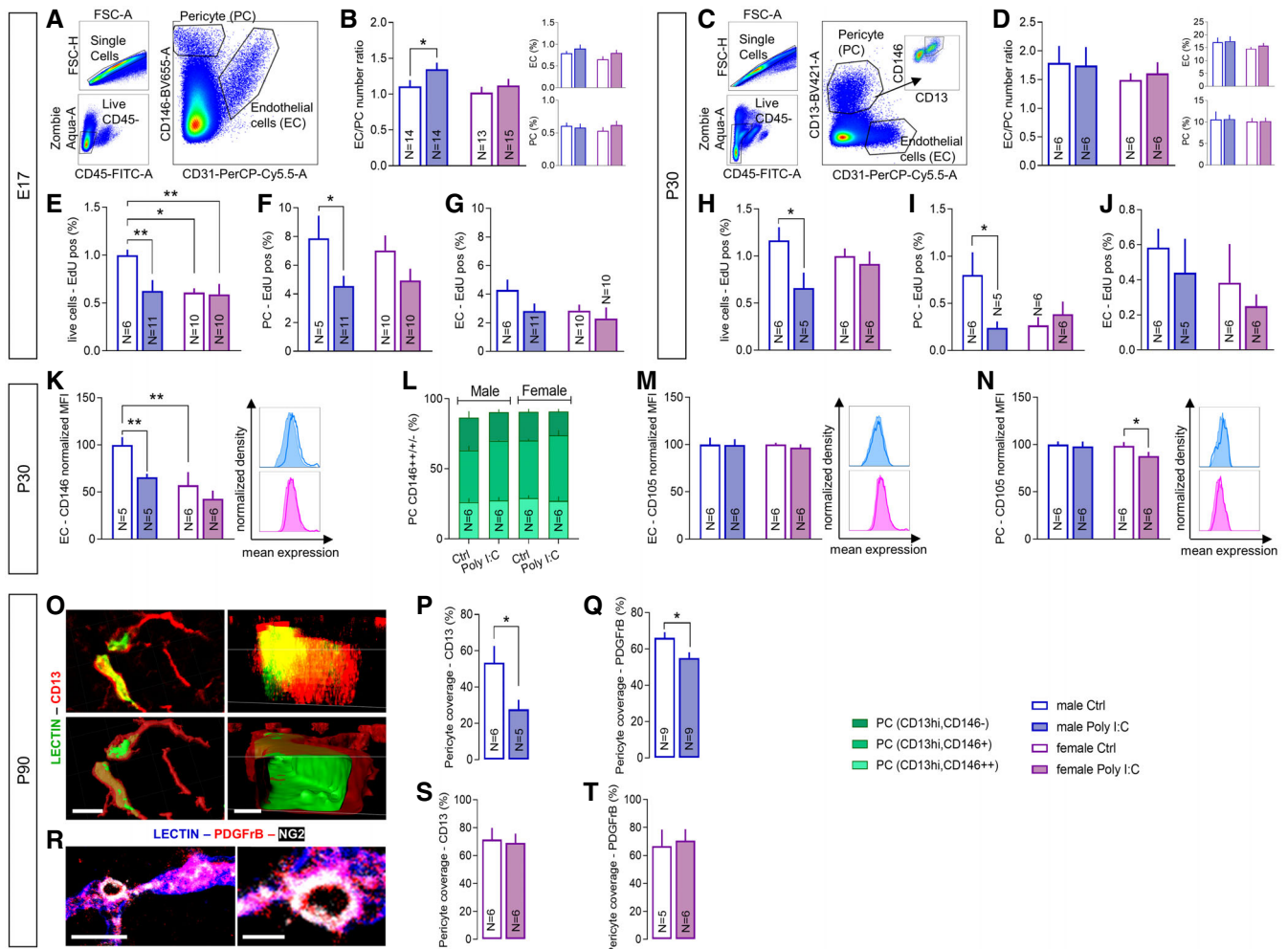


Figure 4.

**Figure 4. Maternal immune activation induces sex-specific alterations of the neurovascular unit changing the ratio between ECs and PCs.**

- A [left] Representative dot plots showing the gating strategy for E17 samples to distinguish NVU cells. The cells were pre-gated on single cells and live cells (Zombie Aqua negative). Live cells were pre-gated on CD45 (CD45<sup>-</sup>). [right] Brain pericytes (PC) were defined as CD146<sup>+</sup>CD31<sup>-</sup> cells and brain endothelial cells (EC) as CD31<sup>+</sup> cells.
- B [left] Quantification of the ratio between PC number and EC numbers for male (blue) and female (purple) E17 offspring cortex samples. Male Ctrl = 1.10 ± 0.08, male Poly I:C = 1.34 ± 0.09, female Ctrl = 1.02 ± 0.08, and female Poly I:C = 1.12 ± 0.09. Mann–Whitney *U*-test, \**P* < 0.05. Bars represent average ratio of individual embryos ± SEM, and numbers in bars indicate the number of embryos. [right up] Percentages of ECs in male Ctrl (0.79 ± 0.05), male Poly I:C (0.90 ± 0.09), female Ctrl (0.65 ± 0.07), and female Poly I:C (0.80 ± 0.07) samples, and [right down] PCs in male Ctrl (0.60 ± 0.05), male Poly I:C (0.57 ± 0.06), female Ctrl (0.53 ± 0.07), and female Poly I:C (0.62 ± 0.06) samples.
- C [left] Gating strategy used to analyze P30 samples: single cells, live (Zombie Aqua negative), and CD45<sup>-</sup> cells. [right] PCs are identified as CD146<sup>+</sup>CD13<sup>+</sup>CD31<sup>-</sup>; and ECs are CD13<sup>-</sup>CD31<sup>+</sup>.
- D [left] Quantification of EC/PC number ratio for male and female P30 offspring cortex samples, obtained by manual gating. Male Ctrl = 1.78 ± 0.29, male Poly I:C = 1.74 ± 0.32, female Ctrl = 1.49 ± 0.11, and female Poly I:C = 1.60 ± 0.19. [right up] Percentages of ECs in male Ctrl (17.07 ± 1.88), male Poly I:C (17.52 ± 1.90), female Ctrl (14.58 ± 0.66), and female Poly I:C (15.73 ± 1.07) samples, and [right down] percentage of PCs in male Ctrl (10.55 ± 1.89), male Poly I:C (10.67 ± 1.04), female Ctrl (10.07 ± 0.85), and female Poly I:C (10.20 ± 0.79).
- E Normalized percentage of live (CD45<sup>-</sup>) EdU-positive cells at E17 in male Ctrl (1.00 ± 0.05), male Poly I:C (0.62 ± 0.11), female Ctrl (0.61 ± 0.04), and female Poly I:C (0.59 ± 0.11) samples. Mann–Whitney *U*-test and Kruskal–Wallis test, \*\**P* < 0.05, \*\*\**P* < 0.001.
- F Percentage of PCs EdU-positive cells at E17 in male Ctrl (7.88 ± 1.57), male Poly I:C (4.55 ± 0.70), female Ctrl (7.03 ± 1.04), and female Poly I:C (4.93 ± 0.83) samples. Student's *t*-test, \**P* < 0.05.
- G Percentage of ECs EdU-positive cells at E17 in male Ctrl (4.30 ± 0.71), male Poly I:C (2.80 ± 0.53), female Ctrl (2.84 ± 0.43), and female Poly I:C (2.29 ± 0.77) samples.
- H Normalized percentage of live (CD45<sup>-</sup>) EdU-positive cells at P30 in male Ctrl (1.16 ± 0.14), male Poly I:C (0.66 ± 0.16), female Ctrl (1.00 ± 0.08), and female Poly I:C (0.91 ± 0.13) samples. Mann–Whitney *U*-test, \**P* < 0.05.
- I Percentage of PCs EdU-positive cells at P30 in male Ctrl (0.80 ± 0.24), male Poly I:C (0.24 ± 0.06), female Ctrl (0.26 ± 0.08), and female Poly I:C (0.38 ± 0.13) samples. Mann–Whitney *U*-test, \**P* < 0.05.
- J Percentage of ECs EdU-positive cells at P30 in male Ctrl (0.58 ± 0.10), male Poly I:C (0.44 ± 0.19), female Ctrl (0.38 ± 0.22), and female Poly I:C (0.25 ± 0.06) samples.
- K [left] CD146-normalized MFI of the EC cells at P30 in male Ctrl (100.00 ± 8.27), male Poly I:C (65.73 ± 3.63), female Ctrl (57.08 ± 14.10), and female Poly I:C (43.07 ± 8.34). Mann–Whitney *U*-test and ordinary one-way ANOVA, \*\**P* < 0.01. [right] Representative histograms CD146 expression on ECs in male Ctrl (blue hollow), male Poly I:C (solid light blue), female Ctrl (purple hollow), and female Poly I:C (solid purple) samples.
- L Percentages of PC CD146<sup>++</sup>, CD146<sup>+</sup>, and CD146<sup>-</sup> cells, respectively, at P30 in male Ctrl (26.32/36.75/23.48 ± 2.84/3.31/4.62), male Poly I:C (27.53/42.40/20.60 ± 2.25/0.58/1.94), female Ctrl (29.05/40.98/2.19 ± 1.99/1.32/2.19), and female Poly I:C (27.17/46.60/17.10 ± 3.09/3.86/1.96) samples.
- M [left] CD105-normalized MFI of the EC cells at P30 in male Ctrl (100.00 ± 7.39), male Poly I:C (99.58 ± 6.23), female Ctrl (100.30 ± 1.61), and female Poly I:C (96.67 ± 3.72). [right] Representative histograms indicating mean fluorescence intensity (MFI) of CD105 on EC in male Ctrl (blue hollow), male Poly I:C (solid light blue), female Ctrl (purple hollow), and female Poly I:C (solid purple) samples.
- N [left] Quantitative data of the normalized MFI of CD105 in PCs at P30 in male Ctrl (100.00 ± 3.43), male Poly I:C (98.01 ± 5.14), female Ctrl (98.57 ± 4.16), and female Poly I:C (87.99 ± 4.21). Mann–Whitney *U*-test, \**P* < 0.05. [right] Representative histograms for CD105 expression on PCs in male Ctrl (blue hollow), male Poly I:C (solid light blue), female Ctrl (purple hollow), and female Poly I:C (solid purple) samples.
- O [top] Representative images of CD13 (red) positive pericytes covering lectin-positive vessels (green) in sections of P90 untreated male brains. [bottom] 3D rendering, scale bar = 20 μm, and enlargement scale bar = 10 μm.
- P Percentage of CD13-positive pericyte coverage at P90 in male Ctrl (53.42 ± 9.22) and Poly I:C (27.73 ± 5.29). Student's *t*-test, \**P* < 0.05.
- Q Percentage of PDGFRβ-positive pericyte coverage at P90 in male Ctrl (66.15 ± 3.09) and Poly I:C (55.08 ± 3.10). Student's *t*-test, \**P* < 0.05.
- R Representative images of PDGFRβ (red) and NG2 (white)-positive pericytes covering lectin-positive vessels (blue) in sections of P90 untreated male brains. Scale bar = 10 μm and enlargement scale bar = 5 μm.
- S Percentage of CD13-positive pericyte coverage at P90 in female Ctrl (71.57 ± 8.37) and Poly I:C (69.13 ± 6.63).
- T Percentage of PDGFRβ-positive pericyte coverage at P90 in female Ctrl (66.77 ± 11.76) and Poly I:C (70.56 ± 8.32).

Data information: Embryos prenatally exposed to vehicle (Ctrl) or Poly I:C on GD9 were dissected, and cortex single-cell suspension was analyzed by multi-color flow cytometry. Ctrl males = white bars with blue border. Poly I:C males = blue bars with blue border. Ctrl females = white bars with purple border. Poly I:C females = purple bars with purple border. CD13-positive pericytes were represented as CD146<sup>-</sup> (dark green bars), CD146<sup>+</sup> (green bars), and CD46<sup>++</sup> (light green bars). Bars represent mean ± SEM, and numbers in bars indicate the number of animals. Source data are available online for this figure.

(Fig 4K). Conversely, PCs isolated at P30 did not display alterations following Poly I:C treatment (Fig 4L), in any of the three identified CD146 subpopulations (i.e., CD146<sup>++</sup>/<sup>+</sup>/<sup>-</sup>, see Appendix Fig S5C). The MFI of CD105 did not show any significant variation in ECs (Fig 4M) with Poly I:C female offspring displaying a small, although significant, reduction in the marker expression in the PC population (Fig 4N) relative to control. Of note, at E17, Poly I:C female offspring showed a decreased CD105 MFI on the ECs (Appendix Fig S5D) compared to controls, possibly suggesting a slower angiogenesis process at this stage. Furthermore, the analysis of CD105 MFI on E17 PCs revealed a sexual dimorphism under physiological conditions, with female PCs displaying a higher expression of CD105 compared to the PCs retrieved from control

males (Appendix Fig S5E). CD105 and CD146 MFI values of the two CD146 positive PC subpopulations are illustrated in Appendix Fig S5F and G.

The reduced PCs proliferation rate in Poly I:C male offspring (Fig 4F and I), along with the lower level of CD146 expression in ECs (Fig 4K), may be at the origin of the defective communication between ECs and PCs, resulting in a functional mismatch in the building of the brain vessels. To investigate this possibility, we analyzed the pericyte coverage of the blood vessels in the cortical region of adult MIA offspring at P90 (Fig 4O–T). The analysis was performed on brain sections stained for lectin (EC marker) and CD13 (PC marker) (Fig 4O) or lectin and PDGFRβ (PC marker) and NG2 (PC and oligodendrocyte progenitor cells shared marker)

(Fig 4R). Quantification of the pericyte area overlapping the vessel revealed that Poly I:C male (Fig 4P and Q), but not female (Fig 4S and T), offspring have a defect in pericyte coverage. Of note, no differences in the amount of collagen type IV were found in the cortex area at P90 for either sex (Appendix Fig S5H–J). Our data indicate a significant reduction in pericyte coverage in Poly I:C-exposed males—but not females—at P90.

**MIA male offspring show intracerebral acute and chronic bleedings**

Pericytes physiologically envelop the brain–blood vessels with a coverage of 60 to 80% (Armulik et al, 2005; Winkler et al, 2012) and their paucity can lead to vascular instability and bleeding phenomena (Armulik et al, 2010). To assess if the Poly I:C male offspring suffer from acute and chronic intracerebral bleedings, we stained brain sections of P30 and P90 mice for hemoglobin (Hb)—a red blood cells marker—and non-heme iron (Fe<sup>3+</sup>) by the Perls staining. Non-heme iron accumulates and gets detectable following

red blood cells and hemoglobin degradation (Morris et al, 1992). The hemoglobin staining performed at P30 (Fig 5A) and P90 (Fig 5B) revealed the occurrence of active intracerebral bleeding at both the investigated ages in Poly I:C male offspring, with no difference in the amount of bleeding between the two postnatal stages (Fig 5C). Similarly, the Perls staining, enhanced by DAB on the P30 slices, showed the accumulation of iron residues within the parenchymal tissues of the Poly I:C male offspring at both P30 (Fig 5D–F) and P90 (Fig 5G and H). Quantification of the DAB-enhanced Perls signal (brown) at P30 (Fig 5E) and the Perls signal (blue) at P90 (Fig 5H) indicated a significant amount of iron deposits into the brain of the MIA-Poly I:C male progeny.

Brains from P30 mice have been virtually reconstructed and the stained sections rendered into a tridimensional volume (Fig 5D and Video S1). The intense signal, produced by the combined Perls + DAB staining, was automatically detected and used to determine the position of each iron deposit/blood spot. Data were then used to perform a points pattern analysis (PPA) along the three anatomical planes (Figs 5F and S6A and B) to investigate the hemorrhages

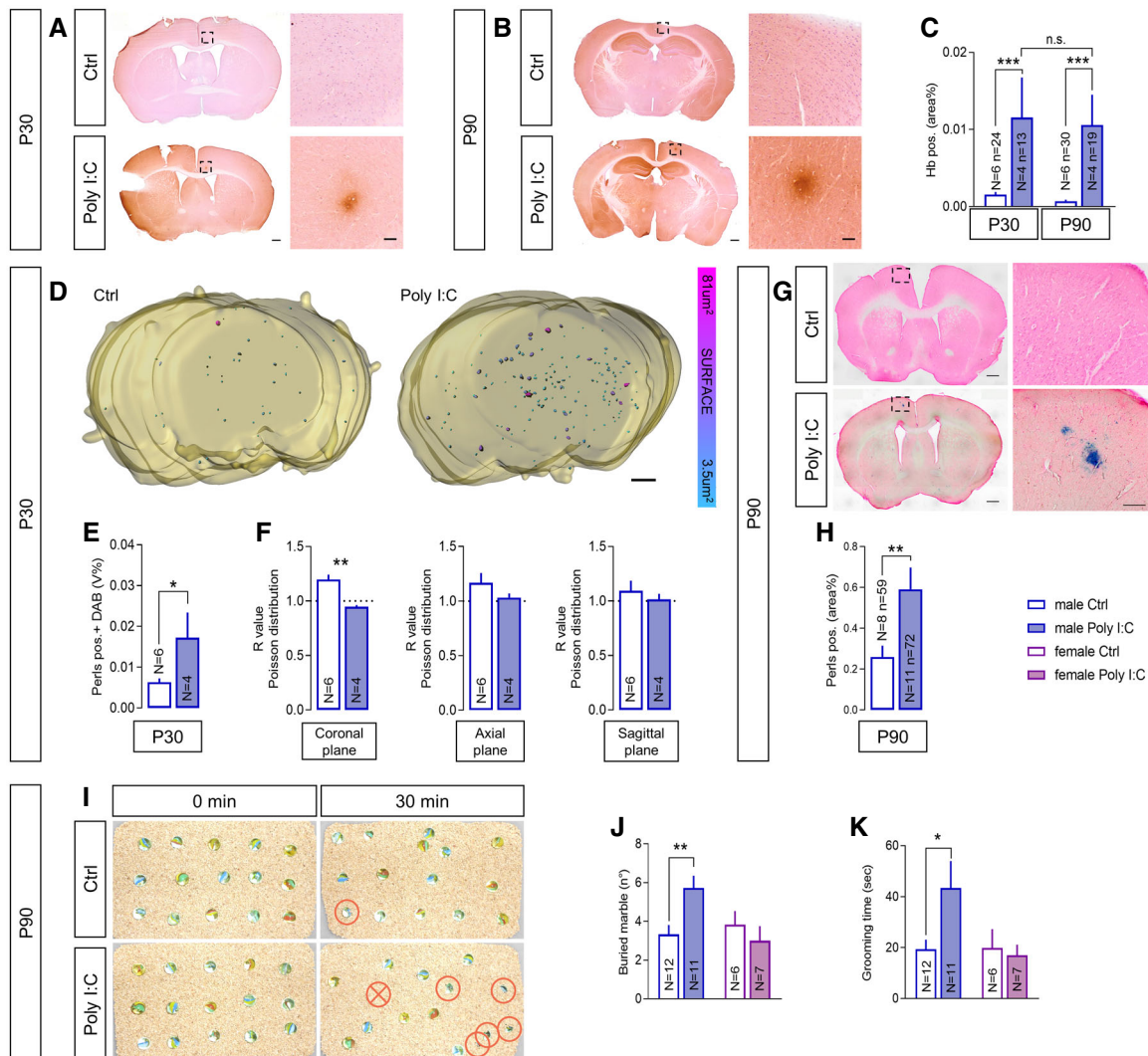


Figure 5.

**Figure 5. MIA-Poly I:C causes acute and chronic intracerebral bleedings.**

- A Representative images of brain acute bleedings detected through hemoglobin IHC in P30 Ctrl and Poly I:C MIA male offspring. Scale bar = 500  $\mu$ m and enlargement scale bar = 50  $\mu$ m.
- B Representative images of brain acute bleedings detected through hemoglobin IHC in P90 Ctrl and Poly I:C MIA male offspring. Scale bar = 500  $\mu$ m and enlargement scale bar = 50  $\mu$ m.
- C Quantification of hemoglobin (Hb)-positive signal in the brain of P30 and P90 male MIA offspring, expressed as a percentage of the area. P30 Ctrl = 0.00  $\pm$  0.00, P30 Poly I:C = 0.01  $\pm$  0.00, P90 Ctrl = 0.00  $\pm$  0.00, and P90 Poly I:C = 0.01  $\pm$  0.00. Mann–Whitney *U*-test, \*\*\**P* < 0.001.
- D Representative 3D rendering of iron deposits detected by DAB-enhanced Perls staining in P30 Ctrl and Poly I:C MIA male offspring brains. Brain volume is rendered gold transparent with a positive signal for the staining color coded by surface dimension. Scale bar = 100  $\mu$ m.
- E Quantification of DAB-enhanced histochemical iron stains in the brain of P30 Ctrl (0.00  $\pm$  0.00) and Poly I:C (0.01  $\pm$  0.00) male MIA offspring, expressed as Perls-positive percentage of the volume. Mann–Whitney *U*-test, \**P* < 0.05.
- F Poisson distribution *R*-value of Perls/DAB-positive staining of P30 male MIA offspring, respectively, in the coronal (Ctrl = 1.19  $\pm$  0.04, Poly I:C = 0.94  $\pm$  0.01; Mann–Whitney *U*-test, \*\**P* < 0.01), axial (Ctrl = 1.16  $\pm$  0.08, Poly I:C = 1.03  $\pm$  0.03), and sagittal (Ctrl = 1.09  $\pm$  0.09, Poly I:C = 1.01  $\pm$  0.05) planes.
- G Representative images of iron deposits detected through Perls staining in P90 Ctrl and Poly I:C MIA male offspring brains. Scale bar = 500  $\mu$ m and enlargement scale bar = 100  $\mu$ m.
- H Quantification of Perls-positive staining in the brain of P90 Ctrl (0.25  $\pm$  0.05) and Poly I:C (0.59  $\pm$  0.10) male MIA offspring, expressed as a percentage of the area. Mann–Whitney *U*-test, \*\**P* < 0.01.
- I Representative image of marble-burying test at 0 and 30 min. Fifteen-glass marbles were evenly spaced on a 5  $\times$  3 grid. Marbles buried by two-thirds at least are indicated by a red circle or by a cross within a red circle when fully covered by the sawdust.
- J Quantification of buried marble (*n*) by P90 Ctrl male (3.33  $\pm$  1.67), Poly I:C male (5.72  $\pm$  2.10), Ctrl female (3.83  $\pm$  1.72), and Poly I:C female (3.00  $\pm$  2.00) mice. Student's *t*-test, \*\**P* < 0.01.
- K Quantification of self-grooming time (sec) by P90 Ctrl males (19.34  $\pm$  13.00), Poly I:C males (43.38  $\pm$  35.21), Ctrl females (19.86  $\pm$  18.06), and Poly I:C females (16.93  $\pm$  11.19) mice. Student's *t*-test, \**P* < 0.05.

Data information: Ctrl males = white bars with blue border. Poly I:C males = blue bars with blue border. Ctrl females = white bars with purple border. Poly I:C females = purple bars with purple border. Numbers in bars indicate the number of animals (*N*) and slices (*n*). Bars represent mean  $\pm$  SEM. Source data are available online for this figure.

distribution inside the brain. The *R* values of the nearest-neighbor analysis, calculated along the different planes, show that the iron deposits of the Poly I:C male offspring are clustered along the coronal plane while possessing a Poisson pattern along the axial and sagittal planes (Fig 5F). No apparent gradient has been found in the distribution of the blood spots along the anatomical axes. These data indicate that the iron deposits, besides being more abundant in the Poly I:C male mice brains (Fig 5E), are grouped closer than stochastically admitted on the coronal plane, suggesting a possible embryological origin of the defect. Graphical representations of the observed and expected nearest neighbors' distances and Kernel density maps of the P30 iron deposits in the three anatomical planes are shown in Appendix Fig S6A and B, respectively. Sections from P30 male mice stained for iron deposits were additionally analyzed by manually segmenting the main brain areas (i.e., olfactory bulb, cortex, hippocampus, caudate–putamen, and thalamus) and the amounts of iron deposits for each area were determined (Appendix Fig S6C). No statistical difference was observed among the different areas in terms of iron deposits volume percentage (V %). Of note, the cortex and the thalamus were the most affected area. The occult blood test on stool samples revealed that the bleeding phenomenon is not generalized and does not affect the gastrointestinal system of P30 and P90 Poly I:C male offspring (Appendix Fig S6D and E). These data indicate that Poly I:C male mice show both acute (Fig 5A–C) and chronic (Fig 5D–H) intracerebral bleedings as a consequence of the MIA protocol.

Interestingly, behavioral analyses through marble burying (Fig 5I and J) and spontaneous grooming (Fig 5K) tests in Poly I:C progeny showed anxiety-related and autistic-like stereotyped repetitive behaviors typical of neuropsychiatric disorders in males. On the other hand, Poly I:C female's offspring were indistinguishable from the controls. Furthermore, taking advantage of the SFARI database for human genes implicated with autism susceptibility, we

evaluated selected cytokine pathways involved in the MIA process that emerged from our results. Enrichment analysis of the relationship between neurodevelopmental diseases and selected cytokine pathways known to participate in the MIA process shows that TGF- $\beta$  has the strongest association with autism and schizophrenia (Appendix Fig S7); few genes expressed in the brain tissue are even both differentially expressed between sexes and correlated with autism and schizophrenia (Appendix Fig S8).

## Discussion

Although anomalies in blood vessel formation are known to result in long-lasting consequences and impairments in brain maturation, the origins of these anomalies are still not fully clarified. We have previously hypothesized that inflammatory events consequent to viral infections during the gestational period could act as potential primary triggers for brain vasculature damage (Rasile et al, 2021). In this study, we provide a direct demonstration that this is the case.

The use of MIA models to investigate the functional outcomes of inflammation during pregnancy, and their underpinning molecular mechanism, has provided the scientific community with invaluable data in recent years (Estes & McAllister, 2016; Corradini et al, 2018). Besides possessing construct, face, and predictive validity, the MIA models revealed the occurrence of sex-specific phenotypes (Hui et al, 2018; Lins et al, 2018; Carlezon et al, 2019; Missig et al, 2019), thus supporting the sex differences observed in human neurodevelopmental diseases (McCarthy et al, 2012; Pinares-Garcia et al, 2018), with males being diagnosed with ASD and schizophrenia, respectively, 4.5 and 1.4 times more frequently than females (Picchioni & Murray, 2007; Bale et al, 2010). Several concomitant events are thought to be the basis of the increased susceptibility to

neurodevelopmental diseases upon maternal immune activation (Haddad et al, 2020; Han et al, 2021). Interestingly, however, accumulating evidence suggests that anomalies of the vasculature are involved in the pathogenesis of neurodevelopmental disorders (Kealy et al, 2020; Rasile et al, 2021). We demonstrate here that MIA, applied in a developmental time window corresponding to angiogenesis, BBB formation, and neurogenesis (Vasudevan et al, 2008), results in altered blood vessel formation and BBB maturation. Our data are in line with evidence published while this manuscript was under revision (Zhao et al, 2022). We also demonstrate the sex selectivity of the above defects and show that they associate with male-specific intracerebral bleedings and repetitive behavior typical of neurodevelopmental diseases. Although we have no direct proof that the behavioral defects are the direct consequence of the altered vessel maturation, it has to be noted that the MIA protocol that we employed does not induce microglia alterations (Corradini et al, 2018), thus minimizing the possibility that the observed defects are the consequence of a generalized inflammatory event. Consistently, upon a single intrauterine exposure to 2 mg/kg Poly I:C at GD9, a selective elevation of TGF- $\beta$  and IL-1 $\beta$  was detected, the latter persisting for only a few hours after the stimulus application.

We also show that the MIA paradigm significantly alters the early endothelium–pericyte interplay mediated by CD146. CD146—also known as MCAM, S-endo-1, P1h12, MUC18, gicerin, or HEMCAM—is a member of the adhesion molecules of the immunoglobulin superfamily (Lehmann et al, 1989). It has a pivotal role in vascular development that has been extensively demonstrated in zebrafish morphant, where it determines blood vessels with the narrowed lumen and leakiness of large molecules (70 kDa) through the BBB (Chan et al, 2005; Chen et al, 2018). Moreover, CD146<sup>EC-KO</sup> mice display impaired BBB formation, with albumin leakiness and low claudin-5 expression (Chen et al, 2017), which identifies claudin-5 as a downstream mediator of CD146 alterations in ECs. Accordingly, we found that MIA male offspring display the presence of narrow vessels, a low expression of the TJs proteins, claudin-5 and ZO-1, and high permeability of the NVU to albumin in MIA-Poly I:C. In line with literature evidence, showing that epithelial cells harvested from organs displaying a leaky barrier retain their defects even upon maintenance *in vitro* (Akdis, 2021), the MIA-Poly I:C-induced barrier anomalies were detectable in vascular cells sorted from prenatally exposed males but not females. The occurrence of sex dimorphisms in vascular cells, even under control conditions (Addis et al, 2014; Lorenz et al, 2015), is emphasized by the differential expression of CD146 between males and females on ECs at P30.

Consistently, our data show that males, but not females, react to MIA-Poly I:C with dysregulation of several transcripts, which are known to be linked with blood vessel development and pericyte contribution to barrier formation. Of interest is the altered expression of Foxf2 in males at E17, since either excessive or low levels of Foxf2 can alter the pericyte number and vascular coverage, leading to albumin extravasation (Reyahi et al, 2015). Moreover, the increase in VEGFa expression, which is influenced by metabolic stress such as hypoxia and hypoglycemia (Shweiki et al, 1992; Stein et al, 1998), indicates that Poly I:C embryos suffer from metabolic stress, which could be linked to the observed increase in blood vessels number. Of note, a similar phenotype has already been described in the autistic brain (Azmitia et al, 2016).

Among the main pathways activated by prenatal Poly I:C, we found TGF- $\beta$  and IL-1 $\beta$  of particular relevance, being responsible for several of the key phenotypes observed in MIA male offspring, in line with the literature (Klein & Flanagan, 2016; Chamera et al, 2020; Posillico et al, 2021). We show here that MIA, induced by exposure to Poly I:C at GD9, not only increases mRNA for TGF- $\beta$  selectively in males but also induces an increment of the active form of TGF- $\beta$ 1, which is able to bind cell surface receptors (Robertson & Rifkin, 2016). Of note, TGF- $\beta$  paracrine signal regulates the interaction between ECs and PCs (Carvalho et al, 2007; Obermeier et al, 2013), with pericyte-secreted TGF- $\beta$  dampening the expression of CD146 on ECs (Chen et al, 2017). Conversely, pericytes constitutively and stably express CD146 (Chen et al, 2017). Of note, our evidence that Poly I:C-mediated TGF- $\beta$  elevation could be prevented in IL-1R KO mice demonstrates a regulatory role played by IL-1 $\beta$  in the phenomenon. Hence, our data suggest that the precocious and abnormal rise of TGF- $\beta$ , probably triggered by IL-1 $\beta$ , likely disrupts the interplay between these cell types, leading to a premature downregulation of CD146 on ECs.

The key role of TGF- $\beta$ 1 in vascular defects manifestation consequent to Poly I:C prenatal challenge is recapitulated by the *in vitro* experiments where the cytokine not only induces the downregulation of CD146 and claudin-5 expression but also alters BBB functional features. Notably, TGF- $\beta$  synergizes with IL-1 $\beta$  in reducing CD146 ECs expression. IL-1 $\beta$  is known to interact with the TGF- $\beta$  signaling, resulting in an unbalance of ALK1/ALK5 activation (Roman-Blas et al, 2007; Luo et al, 2009). In our experimental setting, we detected high activation of ALK1 and unchanged ALK5 activation, thus pointing to specific activation of the TGF- $\beta$  signaling in ECs. SMAD1/5 phosphorylation is indeed mediated by ALK1, which is predominantly expressed in ECs (Armulik et al, 2005; González-Núñez et al, 2013). The *in vitro* experimental setting also allowed us to demonstrate that female-derived ECs respond to TGF- $\beta$ 1 alone, and/or to a combination of IL-1 $\beta$  and TGF- $\beta$ 1, comparably to males. These data exclude the intrinsic resilience of female cells to the cytokines analyzed and further confirm that the sex-specific pathological phenotype results from the lack of cytokine elevation in females prenatally exposed to Poly I:C.

Several literature evidence point to a key effect of TGF- $\beta$  on vascular homeostasis and disease association. The TGF- $\beta$  pathway upregulation in endothelial cells, occurring in GLUT10 deficiency (Coucke et al, 2006) and Loeys-Dietz syndrome (Loeys et al, 2005), weakens the structure of the blood vessels leading to aortic aneurysms associated with arterial tortuosity. In pericytes, the overabundance of active TGF- $\beta$  results in premature cytotaxis: *in vitro* TGF- $\beta$ 1 treatment reduces the proliferative rate of pericytes with no effect on vitality (Khanna, 2004; Rustenhoven et al, 2016), and the same happens in emilin-1 KO mice, which have an excessive level of active TGF- $\beta$  resulting from the increased conversion of pro-TGF $\beta$  to the mature form (Zacchigna et al, 2006). Furthermore, TGF- $\beta$ 1 chronic overproduction causes the dropout of mural cells and reduced coverage of the cerebral vessels (Kato et al, 2020). In accordance with these observations, our data show that MIA male offspring, specifically displaying TGF- $\beta$  signaling upregulation, have a low *in vivo* pericyte proliferative rate at both E17 and P30 and, consequently, a low pericyte coverage of the cerebral blood vessels in the adult age (P90). Furthermore, claudin-5, one of the most important and highly expressed TJ proteins of the NVU (Ohtsuki

*et al.*, 2008), is regulated by PCs presence (Armulik *et al.*, 2010; Bell *et al.*, 2010; Daneman *et al.*, 2010).

The upregulation of the TGF- $\beta$  pathway results in vessels prone, both acutely and chronically, to bleedings. The occurrence of brain bleedings has been previously reported to associate with pericyte paucity, which causes intraventricular hemorrhages of the germinal matrix (GH-IVH) in prematurely born babies (Braun *et al.*, 2007). Moreover, the occurrence of hemorrhagic events, together with low levels of CD146, has been linked to the occurrence of neuropsychiatric diseases (Greene *et al.*, 2019; Rasile *et al.*, 2021). Perinatal brain hemorrhages are a risk factor for schizophrenia (Rosanoff *et al.*, 1934; Torrey *et al.*, 1975) and indeed the injection in mouse fetuses of the pro-hemorrhagic agent lysophosphatidic acid (LPA) induces schizophrenic-like behaviors in experimental animals (Mirendil *et al.*, 2015). Furthermore, a large number of schizophrenic patients suffer from small vessel diseases and up to 50% of them die from cardiovascular diseases (Ringen *et al.*, 2014). Recently, it has been shown that models of MIA, besides exhibiting higher susceptibility to neuropsychiatric disorders, also display a higher incidence of blood pressure alterations and cardiovascular deficits (Deng *et al.*, 2018). Besides being congruent with the occurrence of repetitive behavioral defects in male GD9 Poly I:C offspring, these data are also in line with our analysis of the relationship between neurodevelopmental diseases and the cytokine pathways known to participate in the MIA process, showing that TGF- $\beta$  has the strongest association with autism and schizophrenia.

The existence of a specific time window for the harmful effects of MIA is in line with the concept that NVU maturation is a finely tuned temporally regulated process. This time window seems to correspond to the end of the first trimester of pregnancy, i.e., the beginning of cerebral angiogenesis, when maternal viral infections and inflammation can impair the normal communication between ECs and PCs, thus resulting in male-specific alterations of the NVU. Our work calls for new studies on the consequences of neurovascular damages following large-scale maternal viral infections such as the COVID-19 pandemic.

## Materials and Methods

### Animals and MIA model

Animals were maintained in an SPF animal house with constant temperature and humidity, under a regular light–dark schedule (lights on 7 a.m. to 7 p.m.) and *ad libitum* food and water. All the experimental procedures followed the guidelines established by the European Legislation (Directive 2010/63/EU) and the Italian Legislation (L.D. no 26/2014). MIA was performed as previously described (Corradini *et al.*, 2018). Briefly, pregnant C57BL/6 WT or IL-1R KO mice at GD9 were injected with 2 mg/kg body weight Poly I:C (polyinosinic–polycytidylic acid, Sigma-Aldrich #P9582 lot. 012M4032V) dissolved in saline or vehicle intraperitoneally (i.p.). P20 WT male mice were injected with the same amount of Poly I:C to differentiate between the embryological and adult effects of Poly I:C-induced inflammation. A maximum of three offspring animals for each sex have been analyzed from the same pregnancy. The pool of analyzed animals was derived from at least two distinct dams. Sex differences have been analyzed and observed within litters.

The Poly I:C lot was characterized for molecular weight through electrophoresis run on bleach agarose gel (Aranda *et al.*, 2012) (Appendix Fig S1A), and LPS contamination by Kinetic-QCLTM Kinetic Chromogenic LAL Assay (Lonza #50-650 U)—estimated in 1–16 pg per injected mouse and RNA purity by 260/280 ratio—values range 1.62–1.64.

### Immunostaining of brain slices

For the immunostaining of brain slices, anesthetized mice (100 mg/kg ketamine and 20 mg/kg xylazine cocktail) were transcardially perfused with 0.9% saline followed by 4% paraformaldehyde dissolved in 0.1 M phosphate buffer. Brains were rapidly extracted from the skull and then either snap frozen or put in 4% paraformaldehyde overnight for post-fixation. Frozen brains were included in a pre-cooled Cryobloc-filled mold and cut into 10- $\mu$ m-thick slices with a Microm HM 520 Cryostat. Post-fixed brains were cut with a VT1000S vibratome (Leica Microsystems) into 50- $\mu$ m-thick slices. Immunostaining was performed by a 45 min RT blocking with 10% normal goat serum, 0.2% Triton X-100, and overnight incubation with specific primary antibodies at 4°C and 1-h incubation with secondary antibodies at RT diluted as listed in Appendix Table S1. Z-stack confocal images were acquired using a Leica SPE confocal microscope equipped with an ACS APO 63X/1.30 oil objective or with Olympus Fluo View FV1000, using a UPLFLN 40x/1.30 or a UPLSAPO 60x/1.35 oil objective (Olympus). Fluorescence image processing and analyses were performed using ImageJ software (National Institute of Health) and/or Bitplane (Imaris 7.4.2). Quantitative analysis of claudin 5 and ZO-1 by IF has been obtained by Bitplane (Imaris) after the automatic segmentation of surfaces. Quantitative analysis of CD13 and PDGFrB-positive pericytes has been expressed as the percentage of coverage of the lectin signal and obtained by Bitplane (Imaris) and NIH Image J software, respectively.

For immunohistochemical staining, free-floating slices were permeabilized with PBS, 3% (v/v) methanol, and 0.1% (w/v) Triton X-100, and treated with 3% (v/v) hydrogen peroxide, while the immuno-detection was performed with an anti-mouse secondary antibody followed by MAC1 Universal HRP-Polymer (Biocare Medical, Pacheco, CA, USA) and DAB (3′DiAminoBenzidine; Biocare Medical, Pacheco, CA, USA) revelation. Slices were mounted and acquired by VS120 DotSlide (Olympus) and the dedicated software OlyVIA. Images processing and analyses were performed using ImageJ software (National Institute of Health).

### DiI vascular staining and analysis

1,1′-Dioctadecyl-3,3′,3′-tetramethylindocarbocyanine perchlorate (DiI) crystal was dissolved in pure ethanol at a concentration of 5.9 mg/ml (50X solution). Immediately before use, DiI working solution was obtained by diluting the 50X DiI into PBS–1.2% glucose which was then vortexed for 1 min. The obtained solution was immediately used to transcardially perfuse P90 mice which were then fixed by 4% paraformaldehyde dissolved in 0.1 M phosphate buffer perfusion. Brains were rapidly extracted from the skull and then put in 4% paraformaldehyde overnight for post-fixation. Post-fixed brains were cut with a VT1000S vibratome (Leica Microsystems) into 50- $\mu$ m-thick slices. After confocal imaging at 20X magnification, 3D reconstruction of the vessels was performed by Bitplane

(Imaris) and analyzed by the Filaments software package. The same analysis was performed on CD31-stained slices from P90 Poly I:C males MIA offspring; for these sets of images a 60X objective was used. For antibody details, see Appendix Table S1.

### Perls staining

Fifty- $\mu$ m-thick brain slices were stained with Prussian Blue dye for iron detection. Briefly, a 20% v/v chloridric acid solution and a 10% w/v potassium ferrocyanide trihydrate (K<sub>4</sub>Fe<sub>4</sub>(CN)<sub>6</sub>·3H<sub>2</sub>O, FW 422.4, Sigma, cat# p-3289) solution made in distilled water were mixed just before use. Slices were incubated in the mix solution for 40 min and then washed three times with PBS 1X. A Nuclear Fast Red counterstaining was performed. To further enhance iron detection, the slices derived from the P30 brains—one of every three slices of the entire brain—were additionally incubated with DAB. Briefly, washed slices were incubated with Triton 0.5%, methanol 3%, hydrogen peroxide, 3% PBS solution for 1 h, and then washed three times with PBS 1X. Next, slices were incubated with DAB for 3 min and then washed with distilled water. Perls staining was likewise performed on spleen slices as a positive control. Slices were mounted and acquired by VS120 DotSlide (Olympus) and the dedicated software OlyVIA. Virtual slices alignment, volume reconstruction, and area segmentation were performed by the TrakEM2 plugin in NIH Image J software and Bitplane (Imaris), respectively. Points pattern analysis (PPA) was performed by PAST 3.21 statistical software with the cartesian coordinates of the iron deposit spots along the craniocaudal, dorsoventral, and left–right axis using nearest-neighbor analysis (convex hull area estimation, wrap-around edge correction, and 16 bins). To compare different brains, each plane has been normalized to 120X, 100Y, and 60Z. The null hypothesis is a random Poisson process where clustered points give  $R < 1$ , Poisson patterns give  $R \sim 1$ , while overdispersed points give  $R > 1$ .

### Western blot analysis

Cortical tissues were collected from E17, P20, and P90 Poly I:C or vehicle prenatally treated offspring. For total protein extraction, samples were homogenized on ice in a glass-Teflon potter using a solubilizing mix composed of sodium dodecyl sulfate 1% (SDS), 62.5 mM Tris–HCl (pH 6.8), and 290 mM sucrose. Protein concentration was estimated using Bicinchoninic Acid Assay (BCA) kit (Thermo Fisher Scientific). For western blot analysis, equal amounts of protein (25  $\mu$ g) were loaded and run on 12% acrylamide gel. Membranes were stained with primary antibodies diluted as listed in Appendix Table S1. Detection was performed with Clarity™ Western ECL Substrate (Bio-Rad) and bands were analyzed through Chemidoc apparatus via ImageLab software (Bio-Rad).

### Sex determination by PCR

DNA extraction was performed from tail tissues through a 15 min incubation at 55°C with 200  $\mu$ l of PBNB buffer (50 mM KCl, 10 mM Tris–HCl pH 8.3, 2.5 mM MgCl<sub>2</sub>, 0.1 mg/ml gelatin, 0.45% v/v Nonidet P40, and 0.45% v/v Tween 20) plus 0.8  $\mu$ g proteinase K. The enzyme was then inactivated by 5 min temperature increase at 95°C and the supernatant was used to perform a PCR with sex-determining region Y (SRY) primers (Appendix Table S2).

### Quantitative RT–PCR

Whole embryos obtained 6 h after the GD9 injection or brain cortices from mice at different developmental stages were used. Samples were homogenized in 500  $\mu$ l of TRI reagent (Zymo Research) for RNA extraction. Total RNA was isolated using the Direct-zol RNA MiniPrep isolation kit (Zymo Research) according to the manufacturer's protocol. The RNA was eluted with 25  $\mu$ l DNase/RNase-free water, quantified using NANODrop 2000c spectrophotometer (Thermo Fisher Scientific), and optical density 260/280 nm ratios were determined. Reverse transcription was performed using 1  $\mu$ g RNA with a High-Capacity cDNA RT kit (Applied Biosystems). Real-time polymerase chain reaction (qRT–PCR) was performed using RT–PCR Vii7 (Applied Biosystems) in a final volume of 10  $\mu$ l for SYBR Green technique (SensiFAST SYBR Lo-ROX, Biorline) and 20  $\mu$ l for TaqMan technique (Gene Expression Master Mix, Life Technologies). Each gene was analyzed at least in duplicate and data analyses were performed with the  $\Delta\Delta$ Ct method. All RNA levels were normalized to GAPDH. Primer sequences are listed in Appendix Table S2.

### ELISA measures

Amniotic fluids were collected from the E17 amniotic sac and rapidly frozen. Under specific dilutions, they were tested with different ELISA kits reported in Appendix Table S1. Tissue—either whole embryos obtained at GD9 or E17 brains—were homogenized with 700  $\mu$ l of ice-cold buffer (sucrose 0.32 M, HEPES 1 mM, MgCl<sub>2</sub> 1 mM, EDTA 1 mM, NaHCO<sub>3</sub> 1 mM, PMSF 0.1 mM, and protease inhibitors) using a Tissue Lyser (Qiagen) for 3 min at 30 Hz. After 15 min of centrifugation at 1,600 g at 4°C, supernatant has been collected and evaluated for cytokine content with the specific kits reported in Appendix Table S1 according to the instructions from the manufacturer. The absorbance was then measured at 450 and 540 nm using Synergy H4 (BioTek). When normalized by protein concentration, protein concentration was estimated using the Bicinchoninic Acid Assay (BCA) kit (Thermo Fisher Scientific).

### Evan's blue permeability assay

A 2% Evan's blue (Sigma-Aldrich, cat. no. E2129, dye content  $\geq 75\%$ ) PBS solution was i.p. injected in the mice at 4 ml/kg. Twenty-four hours after the time of injection, animals were anesthetized with ketamine (100 mg/kg) and xylazine (10 mg/kg), transcardially perfused with 0.9% saline, and the brain was rapidly extracted from the skull. The cerebral tissue was weighed and dried up. When fully dry, the specimens were incubated with 70  $\mu$ l of formamide in agitation at 24°C for 72 h. This process allows the extraction of the dye from the tissue. After 10-min centrifugation at 800 g, the supernatant was collected and loaded into 96-well flat-bottom assay plates (Costar®, Corning Inc). The absorbance was then measured at 620 and 740 nm using Optimax Microplate Reader (Molecular Devices). Relative absorbance units were converted into concentration according to standards.

### Brain endothelial cells and pericytes characterization and isolation by fluorescence-activated cell sorting (FACS)

The isolation procedure of endothelial cells and pericytes from the brain tissues was adapted from Crouch & Doetsch (2018). Briefly,

mice were euthanized and the brain was rapidly dissected. After meninges removal, cortices were isolated and finely minced. The tissue was then digested with 3.5 mg/ml Collagenase/Dispase (Roche) and 2% FBS in PBS 1X at 37 °C for 60 min in a hybridization oven set at max speed rotation. After brief centrifugation, 80 µg of DNase I (Sigma) was added to each sample and a mechanical dissociation step was performed by pipetting. Homogenates were deprived of myelin and purified by a 22% Percoll gradient at 600 g for 20 min at 4°C with no brake. Cells were stained with Zombie aqua reagent and the following antibodies for 15 min at RT in the dark: Anti-mouse—CD45 (Immunotools), CD13, CD146, CD105, and CD31 (all from BD) (Appendix Table S1). After washing, cells were either analyzed on a FACSymphony A5 analyzer (BD Biosciences) or sorted with a FACSARIA III cell sorter (BD Biosciences) equipped with a 100 µm nozzle and a plate voltage set to 2,000 volts. Doublets were excluded from the analysis in an FSC-A vs. FSC-H dot plot, among viable non-hematopoietic cells (Zombie aqua<sup>neg</sup> and CD45<sup>neg</sup> cells), endothelial cells were identified based on CD31 expression while pericytes were defined either as CD146<sup>pos</sup> cells in the embryonic brain or CD13<sup>pos</sup> cells in the postnatal brain. FC data were analyzed by FACSDiva 8.0.1 Software (BD Biosciences).

### EdU cell proliferation assay

5-Ethynyl-2'-deoxyuridine (EdU) (Thermo Fisher) was injected at 55 mg/kg i.p. 5 h before sacrifice in pregnant mice at GD17 or 48 h before sacrifice in mice at P30. Animals were anesthetized, transcardially perfused with 0.9% saline, and the brain was rapidly extracted. The cerebral tissue was processed as described for brain endothelial cells and pericytes isolation by FACS and stained according to the manufacturer's protocol before flow cytometry analysis.

### Cell cultures

The immortalized mouse brain endothelial cells line bEnd.3 [BEND3] (ATCC® CRL2299™) was cultured in Dulbecco's modified Eagle's medium (DMEM) supplemented with 10% heat-inactivated fetal bovine serum (FBS) and 1% penicillin–streptomycin (P/S). The cells were maintained in a humidified cell culture incubator at 37 °C with 5% CO<sub>2</sub> and 95% air. Cultures were grown until confluency and treated when TEER values reached > 100 Ω.cm<sup>2</sup>. The mean TEER of the bEnd.3 cultures used was 167 Ω.cm<sup>2</sup>. Primary cultures of endothelial cells (EC) obtained from individual E17 embryos after FACS sorting were seeded at a concentration of 20,000–100,000 cells per cm<sup>2</sup>, and grown in tissue culture plates coated with 10 µg/ml rat tail collagen type I (lower viscosity; Cultrex) and 3 µg/ml fibronectin (Sigma), in EBM-2 medium (Lonza) supplemented with 2% heat-inactivated fetal bovine serum, 1% penicillin–streptomycin (Lonza), 1.4 µM hydrocortisone (Sigma), 5 µg/ml ascorbic acid (Sigma), 1% chemically defined lipid concentrate (Invitrogen), 10 mM HEPES (Lonza), 5 ng/ml basic fibroblast growth factor (bFGF, Lonza), 10 ng/ml epidermal growth factor (EGF, Lonza), 1.95 µg/ml bovine serum albumin, 10 ng/ml vascular endothelial growth factor (VEGF, Immunotool), and 0.1% insulin-like growth factor (IGF-1, Lonza). Primary cultures of pericytes (PC) obtained from individual E17 mouse embryos after FACS sorting were maintained in culture at a cell concentration of 18,000–45,000 viable cells per cm<sup>2</sup>, in EBM-2

medium (Lonza) supplemented with 2% heat-inactivated fetal bovine serum, 1% penicillin–streptomycin (Lonza), 5 µg/ml ascorbic acid (Sigma), 1% chemically defined lipid concentrate (Invitrogen), 10 mM HEPES (Lonza), 50 ng/ml platelet-derived growth factor-BB (PDGF-BB, Immunotool), and grown in 10 µg/ml rat tail collagen type I (lower viscosity; Cultrex) and 3 µg/ml fibronectin (Sigma)-coated plates (cells isolated from different pups were kept separate) at 37°C in a humidified 5% CO<sub>2</sub> incubator.

For mature primary brain EC, cortices of 2-month-old mice were processed as already described for ECs isolation. ECs were seeded at a concentration of 260,000 cells per cm<sup>2</sup> and grown in tissue culture plates coated with 10 µg/ml rat tail collagen type I (Corning) and 3 µg/ml fibronectin (Sigma) in EBM-2 medium (Lonza) supplemented with 10% heat-inactivated fetal bovine serum, 1% penicillin–streptomycin (Lonza), and 4 µg/ml puromycin (Sigma) for the first 2 days to obtain an almost pure endothelial cells culture. Cultures were grown until confluency and treated when TEER values reached > 90 Ω.cm<sup>2</sup>. The mean TEER of the primary cultures used was 160.5 Ω.cm<sup>2</sup>.

### 3D barrier model

The protocol for the 3D BBB model *in vitro* building was adapted from Lauranzano *et al* (2019). Briefly, PC and EC or bEnd.3 were cultured as a monolayer or co-cultured as a double layer on Transwell® (polycarbonate, 6.5 mm diameter, 3 µm pore size, 24 wells; Corning) coated with 10 µg/ml rat tail collagen type I (lower viscosity; Cultrex) and 3 µg/ml fibronectin (Sigma). PC were seeded onto the abluminal side of the filter, whereas EC or bEnd.3 cells were cultured to confluence onto the luminal side of the membrane. PC and EC or bEnd.3 were co-cultured for 7–14 days at 37°C with 5% CO<sub>2</sub>. For *in vitro* BBBs made of mature primary EC, Transwell® (polycarbonate, 12 mm diameter, 3 µm pore size, 12 wells; Corning) coated with 10 µg/ml rat tail collagen type I (lower viscosity; Cultrex) and 3 µg/ml fibronectin (Sigma) were used.

### Transendothelial cell electrical resistance (TEER) assay

TEER was measured using a Voltometer (Millicell Electrical Resistance System, Millipore). TEER values were recorded in barrier models and cell-free matrix-coated transwells. Absolute TEER values were obtained by subtracting background resistance from barrier resistance values and correcting for the area covered by the cells. TEER was recorded once a day to monitor cell confluence. Variation in absolute TEER for each transwell was measured over time from T<sub>0</sub>, then averaged for each day before treatment and expressed as fold change of control cells.

### *In vitro* barriers model treatment

Before treatment, cells were starved for 24 h by reducing the amount of serum in the media from 5% to 0.5%; this has been done to lower the amount of TGF-β in the culture medium. After starvation, the cells were incubated for up to 72 h with 10 ng/ml IL-1β and/or 10 ng/ml TGF-β1 in a medium with 2% serum. When both cytokines were used, IL-1β was added to the culture 30 min before TGF-β1. IL-1β and/or TGF-β1 were administered to the 3D *in vitro* barrier model in complete media on the basolateral side.



### Ac-LDL uptake assay

DiI-fluorescently labeled acetylated low-density lipoprotein (DiI AcLDL; Thermo Fisher) was diluted in EBM2 medium at a concentration of 10  $\mu\text{g/ml}$  and added to cultured cells for 4 h at 37°C in a humidified 5%  $\text{CO}_2$  incubator. Ac-LDL uptake was analyzed by fluorescence microscopy and acquired with an inverted microscope Olympus IX53 (Center Valley, PA, USA). Alternatively, cells were stained with Diff Quick (Dade Behring, BioMap) and acquired with an inverted microscope Olympus IX53 (Center Valley, PA, USA).

### Dextran permeability assay

Dextran permeability assay was performed as previously described (Lauranzano et al, 2019). Briefly, 10 kDa -Dextran Alexa Fluor<sup>®</sup> 488-conjugated (Thermo Fisher) 10  $\mu\text{g/ml}$  diluted in DMEM FluoroBrite<sup>™</sup> (Life Technologies) was added to the apical compartment of confluent PC-bEnd.3 co-cultures or endothelial monolayers for 1 h at 37°C in a humidified 5%  $\text{CO}_2$  incubator with continuous slow mixing for E17-derived cells. For mature primary ECs, 3 kDa Dextran Alexa Fluor<sup>®</sup> 488-conjugated (Thermo Fisher) 100  $\mu\text{g/ml}$  and 10 kDa Dextran Alexa Fluor<sup>®</sup> 555-conjugated (Thermo Fisher) 10  $\mu\text{g/ml}$  were used instead. Solute paracellular permeability was assessed by measuring the amount of fluorescent tracer in the apical and basolateral compartments using Synergy<sup>™</sup> H4 Hybrid Multi-Mode Microplate Reader (BioTek). Relative fluorescence units were corrected for background fluorescence and converted into concentration according to standards. The amount of fluorescent test compound was calculated as permeability coefficient ( $P_e$ , cm/min), as previously described in detail. The experiments were done at least in triplicates for each condition.

### Immunostaining of cells

Cells were cultured onto round coverslips for this purpose and then fixed with 4% PFA/sucrose for 15 min at RT. Cells were washed with dPBS, permeabilized, and blocked in GSDB 1X solution (15% goat serum, 0.3% Triton X-100, 450 mM NaCl, and 20 mM phosphate buffer pH 7.4) for 1 h at RT, then incubated with primary antibodies o/n at 4°C. The following day, the cells were washed twice with salt solution before incubation with secondary antibodies (diluted 1:500 in permablock) for 1 h in the dark. Coverslips were mounted onto slides with FluorSave Reagent (Calbiochem).

Slides were stored at 4°C until visualized by confocal microscopy. Z-stack confocal images were acquired using a Leica SPE confocal microscope equipped with an ACS APO 63X/1.30 Oil objective or with Olympus Fluo View FV1000, using a UPLFLN 40x/1.30 or a UPLSAPO 60x/1.35 oil objective (Olympus). Fluorescence image processing and analyses were performed using ImageJ software (National Institute of Health) and/or Bitplane (Imaris).

### Detection of occult blood in the stools

Stools from mice at P30 and P90 were collected and tested for the presence of blood through Hemocult Sensa (Mountainside Medical) according to the manufacturer's protocol. Briefly, stools were pressed on precoated cardboard, and the revealing reagent was applied on the backside of the sample square, as well as on the

positive and negative control spots. The appearance of a blue coloration within a couple of minutes on the cardboard indicates the presence of blood in the sample.

### Gene enrichment analysis

We performed an enrichment analysis to verify the involvement of genes in the TGF- $\beta$ , TNF- $\alpha$ , IL-1, and IL-6 pathways with autism and schizophrenia. We obtained the list of genes and connecting genes of each of the four pathways from the SIGNOR 3.0 database (snapshot of December López-Aranda et al, 2021) (Perfetto et al, 2016; Licata et al, 2020). We collected the list of genes implicated in autism susceptibility from the SFARI Gene database (release of September López-Aranda et al, 2021) (Abrahams et al, 2013), and the list of schizophrenia-associated genes obtained in the genome-wide association studies CLOZUK, PGC, and PGC2 (Ripke et al, 2014; Pardiñas et al, 2018; Wu et al, 2020) curated from the Schizophrenia Database (Wu et al, 2020). The list of genes differentially expressed by sex in prenatal and adult brain samples was obtained from Werling et al (2016). We extracted intersections of the identified gene sets and computed the  $P$  values for enrichment with hypergeometric tests (Datasets EV1 and EV2) (Note that the  $P$ -values cannot be taken directly as significance flags, or as a measure of the strength of association, because they rely on databases of known associations, i.e., biased toward the existing literature, thus ignoring associations that are still unreported.)

### Marble burying

The marble burying test measures obsessive-compulsive disorder (OCD) reflecting anxiety-like behavior response. During the test, mice at P90 were placed individually, without food or water, in a clear plastic box containing 15 glass marbles (1.5 cm in diameter) that were evenly spaced on a 5  $\times$  3 grid. The measure of marble-burying behavior was the number of marbles buried to at least two thirds of the depth of the sawdust, within 30 min. The tests were performed in a counterbalanced manner, by direct observation by a trained observer, blind to the treatment. All experiments were conducted between 10 am and 5 pm.

### Self-grooming

Mice at P90 were scored for spontaneous grooming behaviors as described earlier (Silverman et al, 2010) with slight modifications. Each mouse was placed individually into a clean mouse cage with a thin (0.5 cm) layer of bedding reducing neophobia while preventing digging, a potentially competing behavior. After 5 min of acclimatization, each mouse was scored with a stopwatch for 10 min for cumulative time spent grooming all body regions by an expert observer, blind to the treatment. All experiments were conducted between 10 am and 5 pm.

### Statistical analysis

Results are presented as means  $\pm$  SEM. The normal distribution of experimental data was assessed using the D'Agostino-Pearson-Kolmogorov-Smirnov normality test or the Shapiro-Wilk test for small sets of values. To compare two normally distributed sample groups,

we used Student's paired or unpaired test. To compare two sample groups that were not normally distributed, we used Mann–Whitney's nonparametric test. To compare more than two normally distributed sample groups, we used ordinary one-way ANOVA for normally distributed sample groups or Kruskal–Wallis test for not normally distributed sample groups, followed by Tukey's or Sidak's multiple-comparison test. Statistical analyses were performed by using GraphPad 8 (Prism) software. Differences are significant if  $P \leq 0.05$  and are indicated by \*; those at  $P \leq 0.01$  are indicated by \*\*; those at  $P \leq 0.001$  are indicated by \*\*\*; and those at  $P \leq 0.0001$  by \*\*\*\*.

## Data availability

BioStudies accession number S-BIAD530 (<https://www.ebi.ac.uk/biostudies/studies/S-BIAD530>).

**Expanded View** for this article is available [online](#).

## Acknowledgments

We thank Professor William Stallcup (SBP - La Jolla, CA) for providing us with the anti-NG2 antibody raised in the guinea pig. TG thanks Livia Peretto (Human Technopole) for support with the SIGNOR database. This work was supported by PRIN (Ministero dell'Istruzione dell'Università e della Ricerca, #2017A9MK4R), FISM (2019/R-Single/032), FERRING COVID-19 Investigational Grant to MM, and by Ministero della Salute (Grant No. RF-2019-12370972 to MM, and Grant No. GR-2018-12367117 and GR-2019-12370776 to EL).

## Author contributions

**Marco Rasile:** Conceptualization; data curation; formal analysis; investigation; writing – original draft; writing – review and editing. **Eliana Lauranzano:** Formal analysis; investigation; methodology. **Elisa Faggiani:** Data curation; formal analysis. **Margherita M Ravanelli:** Data curation; formal analysis. **Federico S Colombo:** Data curation; formal analysis. **Filippo Mirabella:** Data curation; formal analysis. **Irene Corradini:** Data curation; formal analysis. **Maria L Malosio:** Methodology. **Antonella Borreca:** Data curation; formal analysis. **Elisa Focchi:** Data curation; formal analysis. **Davide Pozzi:** Methodology. **Toni Giorgino:** Data curation; formal analysis. **Isabella Barajon:** Resources; supervision. **Michela Matteoli:** Conceptualization; supervision; funding acquisition; validation; project administration; writing – review and editing.

## Disclosure and competing interests statement

The authors declare that they have no conflict of interest.

## References

- Abrahams BS, Arking DE, Campbell DB, Mefford HC, Morrow EM, Weiss LA, Menashe I, Wadkins T, Banerjee-Basu S, Packer A (2013) SFARI gene 2.0: a community-driven knowledgebase for the autism spectrum disorders (ASDs). *Mol Autism* 4: 36
- Addis R, Campesi I, Fois M, Capobianco G, Dessole S, Fenu G, Montella A, Cattaneo MG, Vicentini LM, Franconi F (2014) Human umbilical endothelial cells (HUVECs) have a sex: characterisation of the phenotype of male and female cells. *Biol Sex Differ* 5: 1–12
- Akdís CA (2021) Does the epithelial barrier hypothesis explain the increase in allergy, autoimmunity and other chronic conditions? *Nat Rev Immunol* 21: 739–751
- Al-Haddad BJS, Jacobsson B, Chabra S, Modzelewska D, Olson EM, Bernier R, Enquobahrie DA, Hagberg H, Östling S, Rajagopal L et al (2019) Long-term risk of neuropsychiatric disease after exposure to infection *in utero*. *JAMA Psychiat* 76: 594–602
- Aranda PS, Lajoie DM, Jorczyk CL (2012) Bleach gel: a simple agarose gel for analyzing RNA quality. *Electrophoresis* 33: 366–369
- Armulik A, Abramsson A, Betsholtz C (2005) Endothelial/pericyte interactions. *Circ Res* 97: 512–523
- Armulik A, Genové G, Mäe M, Nisancioglu MH, Wallgard E, Niaudet C, He L, Norlin J, Lindblom P, Strittmatter K et al (2010) Pericytes regulate the blood-brain barrier. *Nature* 468: 557–561
- Azmitia EC, Saccomano ZT, Alzoobaee MF, Boldrini M, Whitaker-Azmitia PM (2016) Persistent angiogenesis in the autism brain: an immunocytochemical study of postmortem cortex, brainstem and cerebellum. *J Autism Dev Disord* 46: 1307–1318
- Bale TL, Baram TZ, Brown AS, Goldstein JM, Insel TR, McCarthy MM, Nemeroff CB, Reyes TM, Simerly RB, Susser ES et al (2010) Early life programming and neurodevelopmental disorders. *Biol Psychiatry* 68: 314–319
- Bell AH, Miller SL, Castillo-Melendez M, Malhotra A (2019) The neurovascular unit: effects of brain insults during the perinatal period. *Front Neurosci* 13: 1452
- Bell RD, Winkler EA, Sagare AP, Singh I, LaRue B, Deane R, Zlokovic BV (2010) Pericytes control key neurovascular functions and neuronal phenotype in the adult brain and during brain aging. *Neuron* 68: 409–427
- Bowers JM, Waddell J, McCarthy MM (2010) A developmental sex difference in hippocampal neurogenesis is mediated by endogenous oestradiol. *Biol Sex Differ* 1: 8
- Braun A, Xu H, Hu F, Kocherlakota P, Siegel D, Chander P, Ungvari Z, Csiszar A, Nedergaard M, Ballabh P (2007) Paucity of pericytes in germinal matrix vasculature of premature infants. *J Neurosci* 27: 12012–12024
- Brown AS, Derkits EJ (2010) Prenatal infection and schizophrenia: a review of epidemiologic and translational studies. *Am J Psychiatry* 167: 261–280
- Brown AS, Meyer U (2018) Maternal immune activation and neuropsychiatric illness: a translational research perspective. *Am J Psychiatry* 175: 1073–1083
- Carlezon WJ, Kim W, Missig G, Finger BC, Landino SM, Alexander AJ, Mokler EL, Robbins JO, Li Y, Bolshakov VY et al (2019) Maternal and early postnatal immune activation produce sex-specific effects on autism-like behaviors and neuroimmune function in mice. *Sci Rep* 9: 16928
- Carvalho RLC, Itoh F, Goumans M-J, Lebrin F, Kato M, Takahashi S, Ema M, Itoh S, van Rooijen M, Bertolino P et al (2007) Compensatory signalling induced in the yolk sac vasculature by deletion of TGF $\beta$  receptors in mice. *J Cell Sci* 120: 4269–4277
- Chamera K, Kotarska K, Szuster-Głuszczyk M, Trojan E, Skórkowska A, Pomierny B, Krzyżanowska W, Bryniarska N, Basta-Kaim A (2020) The prenatal challenge with lipopolysaccharide and polyinosinic:polycytidylic acid disrupts CX3CL1–CX3CR1 and CD200–CD200R signalling in the brains of male rat offspring: a link to schizophrenia-like behaviours. *J Neuroinflammation* 17
- Chan B, Sinha S, Cho D, Ramchandran R, Sukhatme VP (2005) Critical roles of CD146 in zebrafish vascular development. *Dev Dyn an Off Publ Am Assoc Anat* 232: 232–244
- Chen J, Luo Y, Huang H, Wu S, Feng J, Zhang J, Yan X (2018) CD146 is essential for PDGFR $\beta$ -induced pericyte recruitment. *Protein Cell* 9: 743–747

- Chen J, Luo Y, Hui H, Cai T, Huang H, Yang F, Feng J, Zhang J, Yan X (2017) CD146 coordinates brain endothelial cell–pericyte communication for blood–brain barrier development. *Proc Natl Acad Sci* 114: E7622–E7631
- Coelho-Santos V, Shih AY (2020) Postnatal development of cerebrovascular structure and the neuroglial unit. *Wiley Interdiscip Rev Dev Biol* 9: e363
- Corradini I, Focchi E, Rasile M, Morini R, Desiato G, Tomasoni R, Lizier M, Ghirardini E, Fesce R, Morone D et al (2018) Maternal immune activation delays excitatory-to-inhibitory gamma-aminobutyric acid switch in offspring. *Biol Psychiatry* 83: 680–691
- Coucke PJ, Willaert A, Wessels MW, Callewaert B, Zoppi N, De Backer J, Fox JE, Mancini GMS, Kambouris M, Gardella R et al (2006) Mutations in the facilitative glucose transporter GLUT10 alter angiogenesis and cause arterial tortuosity syndrome. *Nat Genet* 38: 452–457
- Crouch EE, Doetsch F (2018) FACS isolation of endothelial cells and pericytes from mouse brain microregions. *Nat Protoc* 13: 738–751
- Daneman R, Zhou L, Kebede AA, Barres BA (2010) Pericytes are required for blood–brain barrier integrity during embryogenesis. *Nature* 468: 562–566
- Deng Y, Song L, Nie X, Shou W, Li X (2018) Prenatal inflammation exposure-programmed cardiovascular diseases and potential prevention. *Pharmacol Ther* 190: 159–172
- Estes ML, McAllister AK (2016) Maternal immune activation: implications for neuropsychiatric disorders. *Science* 353: 772–777
- Gaengel K, Genove G, Armulik A, Betsholtz C (2009) Endothelial-mural cell signaling in vascular development and angiogenesis. *Arterioscler Thromb Vasc Biol* 29: 630–639
- Gardener H, Spiegelman D, Buka SL (2011) Perinatal and neonatal risk factors for autism: a comprehensive meta-analysis. *Pediatrics* 128: 344–355
- Gardner MR (2005) Outcomes in children experiencing neurologic insults as preterm neonates. *Pediatr Nurs* 31: 451–456
- Goasdoué K, Miller SM, Colditz PB, Björkman ST (2017) Review: the blood–brain barrier; protecting the developing fetal brain. *Placenta* 54: 111–116
- González-Núñez M, Muñoz-Félix JM, López-Novoa JM (2013) The ALK-1/Smad1 pathway in cardiovascular physiopathology. A new target for therapy? *Biochim Biophys Acta - Mol Basis Dis* 1832: 1492–1510
- Greene C, Hanley N, Campbell M (2019) Claudin-5: gatekeeper of neurological function. *Fluids Barriers CNS* 16: 3
- Haddad FL, Patel SV, Schmid S (2020) Maternal immune activation by poly I: C as a preclinical model for neurodevelopmental disorders: a focus on autism and schizophrenia. *Neurosci Biobehav Rev* 113: 546–567
- Han VX, Patel S, Jones HF, Dale RC (2021) Maternal immune activation and neuroinflammation in human neurodevelopmental disorders. *Nat Rev Neurol* 17: 564–579
- Hui CW, St-Pierre A, El Hajj H, Remy Y, Hébert SS, Luheshi GN, Srivastava LK, Tremblay M-È (2018) Prenatal immune challenge in mice leads to partly sex-dependent behavioral, microglial, and molecular abnormalities associated with schizophrenia. *Front Mol Neurosci* 11: 1–14
- Kato T, Sekine Y, Nozaki H, Uemura M, Ando S, Hirokawa S, Onodera O (2020) Excessive production of transforming growth factor  $\beta$ 1 causes mural cell depletion from cerebral small vessels. *Front Aging Neurosci* 12: 151
- Kealy J, Greene C, Campbell M (2020) Blood–brain barrier regulation in psychiatric disorders. *Neurosci Lett* 726: 133664
- Khanna A (2004) Concerted effect of transforming growth factor-beta, cyclin inhibitor p21, and c-myc on smooth muscle cell proliferation. *Am J Physiol Heart Circ Physiol* 286: H1133–H1140
- Kinney DK, Yurgelun-Todd DA, Tohen M, Tramer S (1998) Pre- and perinatal complications and risk for bipolar disorder: a retrospective study. *J Affect Disord* 50: 117–124
- Klein SL, Flanagan KL (2016) Sex differences in immune responses. *Nat Rev Immunol* 16: 626–638
- Knuessel I, Chicha L, Britschgi M, Schobel SA, Bodmer M, Hellings JA, Toovey S, Prinssen EP (2014) Maternal immune activation and abnormal brain development across CNS disorders. *Nat Rev Neurol* 10: 643–660
- Lauranzano E, Campo E, Rasile M, Molteni R, Pizzocri M, Passoni L, Bello L, Pozzi D, Pardi R, Matteoli M et al (2019) A microfluidic human model of blood–brain barrier employing primary human astrocytes. *Adv Biosyst* 3: 1800335
- Lebrin F, Deckers M, Bertolino P, ten Dijke P (2005) TGF- $\beta$  receptor function in the endothelium. *Cardiovasc Res* 65: 599–608
- Lehmann JM, Riethmüller G, Johnson JP (1989) MUC18, a marker of tumor progression in human melanoma, shows sequence similarity to the neural cell adhesion molecules of the immunoglobulin superfamily. *Proc Natl Acad Sci U S A* 86: 9891–9895
- Li F, Lan Y, Wang Y, Wang J, Yang G, Meng F, Han H, Meng A, Wang Y, Yang X (2011) Endothelial Smad4 maintains cerebrovascular integrity by activating N-cadherin through cooperation with notch. *Dev Cell* 20: 291–302
- Licata L, Lo Surdo P, Iannuccelli M, Palma A, Micarelli E, Perfetto L, Peluso D, Calderone A, Castagnoli L, Cesareni G (2020) SIGNOR 2.0, the SIGNaling network open resource 2.0: 2019 update. *Nucleic Acids Res* 48: D504–D510
- Lins BR, Hurtubise JL, Roebuck AJ, Marks WN, Zabder NK, Scott GA, Greba Q, Dawicki W, Zhang X, Rudulier CD et al (2018) Prospective analysis of the effects of maternal immune activation on rat cytokines during pregnancy and behavior of the male offspring relevant to schizophrenia. *eNeuro* 5: ENEURO.0249-18.2018
- Liu P, Zhu Z, Zeng C, Nie G (2012) Specific absorption spectra of hemoglobin at different PO2 levels: potential noninvasive method to detect PO2 in tissues. *J Biomed Opt* 17: 125002
- Loeys BL, Chen J, Neptune ER, Judge DP, Podowski M, Holm T, Meyers J, Leitch CC, Katsanis N, Sharifi N et al (2005) A syndrome of altered cardiovascular, craniofacial, neurocognitive and skeletal development caused by mutations in TGFBR1 or TGFBR2. *Nat Genet* 37: 275–281
- López-Aranda MF, Chattopadhyay I, Boxx GM, Fraley ER, Silva TK, Zhou M, Phan M, Herrera I, Taloma S, Mandanas R et al (2021) Postnatal immune activation causes social deficits in a mouse model of tuberous sclerosis: role of microglia and clinical implications. *Sci Adv* 7: eabf2073
- Lorenz M, Koschate J, Kaufmann K, Kreye C, Mertens M, Kuebler WM, Baumann G, Gossing G, Marki A, Zakrzewicz A et al (2015) Does cellular sex matter? Dimorphic transcriptional differences between female and male endothelial cells. *Atherosclerosis* 240: 61–72
- Luo DD, Fielding C, Phillips A, Fraser D (2009) Interleukin-1 beta regulates proximal tubular cell transforming growth factor beta-1 signalling. *Nephrol Dial Transplant* 24: 2655–2665
- Lydholm CN, Köhler-Forsberg O, Nordentoft M, Yolken RH, Mortensen PB, Petersen L, Benros ME (2019) Parental infections before, during, and after pregnancy as risk factors for mental disorders in childhood and adolescence: a Nationwide Danish study. *Biol Psychiatry* 85: 317–325
- Mackenzie F, Ruhrberg C (2012) Diverse roles for VEGF-A in the nervous system. *Development* 139: 1371–1380
- Mancuso MR, Kuhnert F, Kuo CJ (2008) Developmental angiogenesis of the central nervous system. *Lymphat Res Biol* 6: 173–180
- McCarthy MM, Arnold AP, Ball GF, Blaustein JD, De Vries GJ (2012) Sex differences in the brain: the not so inconvenient truth. *J Neurosci* 32: 2241–2247
- Mirendil H, Thomas EA, De Loera C, Okada K, Inomata Y, Chun J (2015) LPA signaling initiates schizophrenia-like brain and behavioral changes in a mouse model of prenatal brain hemorrhage. *Transl Psychiatry* 5: e541

- Missig G, Robbins JO, Mokler EL, McCullough KM, Bilbo SD, McDougle CJ, Carlezon WA (2019) Sex-dependent neurobiological features of prenatal immune activation via TLR7. *Mol Psychiatry* 25: 2330–2341
- Moretti R, Pansiot J, Bettati D, Strazielle N, Ghersi-Egea J-F, Damante G, Fleiss B, Titomanlio L, Gressens P (2015) Blood-brain barrier dysfunction in disorders of the developing brain. *Front Neurosci* 9: 40
- Morris CM, Candy JM, Oakley AE, Bloxham CA, Edwardson JA (1992) Histochemical distribution of non-haem iron in the human brain. *Acta Anat (Basel)* 144: 235–257
- Nation DA, Sweeney MD, Montagne A, Sagare AP, D'Orazio LM, Pachicano M, Sepeshband F, Nelson AR, Buennagel DP, Harrington MG et al (2019) Blood-brain barrier breakdown is an early biomarker of human cognitive dysfunction. *Nat Med* 25: 270–276
- Obermeier B, Daneman R, Ransohoff RM (2013) Development, maintenance and disruption of the blood-brain-barrier. *Nat Methods* 19: 1584–1596
- Ohtsuki S, Yamaguchi H, Katsukura Y, Asashima T, Terasaki T (2008) mRNA expression levels of tight junction protein genes in mouse brain capillary endothelial cells highly purified by magnetic cell sorting. *J Neurochem* 104: 147–154
- Pardiñas AF, Holmans P, Pocklington AJ, Escott-Price V, Ripke S, Carrera N, Legge SE, Bishop S, Cameron D, Hamshere ML et al (2018) Common schizophrenia alleles are enriched in mutation-intolerant genes and in regions under strong background selection. *Nat Genet* 50: 381–389
- Perfetto L, Briganti L, Calderone A, Cerquone Perpetuini A, Iannucelli M, Langone F, Licata L, Marinkovic M, Mattioni A, Pavlidou T et al (2016) SIGNOR: a database of causal relationships between biological entities. *Nucleic Acids Res* 44: D548–D554
- Picchioni MM, Murray RM (2007) Schizophrenia. *Br Med J* 335: 91–95
- Pinares-García P, Stratikopoulos M, Zagato A, Loke H, Lee J (2018) Sex: a significant risk factor for neurodevelopmental and neurodegenerative disorders. *Brain Sci* 8: 154
- Posillico CK, Garcia-Hernandez RE, Tronson NC (2021) Sex differences and similarities in the neuroimmune response to central administration of poly I:C. *J Neuroinflammation* 18
- Preti A, Cardascia L, Zen T, Pellizzari P, Marchetti M, Favaretto G, Miotto P (2000) Obstetric complications in patients with depression — a population-based case-control study. *J Affect Disord* 61: 101–106
- Rasile M, Lauranzano E, Mirabella F, Matteoli M (2021) Neurological consequences of neurovascular unit and brain vasculature damages: potential risks for pregnancy infections and COVID-19-babies. *FEBS J* 289: 3374–3392
- Reyahi A, Nik AM, Ghiami M, Gritli-Linde A, Pontén F, Johansson BR, Carlsson P (2015) Foxf2 is required for brain pericyte differentiation and development and maintenance of the blood-brain barrier. *Dev Cell* 34: 19–32
- Ringen PA, Engh JA, Birkenaes AB, Dieset I, Andreassen OA (2014) Increased mortality in schizophrenia due to cardiovascular disease - a non-systematic review of epidemiology, possible causes, and interventions. *Front Psych* 5: 137
- Ripke S, Neale BM, Corvin A, Walters JTR, Farh K-H, Holmans PA, Lee P, Bulik-Sullivan B, Collier DA, Huang H et al (2014) Biological insights from 108 schizophrenia-associated genetic loci. *Nature* 511: 421–427
- Robertson IB, Rifkin DB (2016) Regulation of the bioavailability of TGF- $\beta$  and TGF- $\beta$ -related proteins. *Cold Spring Harb Perspect Biol* 8: a021907
- Roman-Blas JA, Stokes DG, Jimenez SA (2007) Modulation of TGF-beta signaling by proinflammatory cytokines in articular chondrocytes. *Osteoarthritis Cartil* 15: 1367–1377
- Rosanoff AJ, Handy LM, Plesset IR, Brush S (1934) The etiology of so-called schizophrenic psychoses. *Am J Psychiatry* 91: 247–286
- Rustenhoven J, Alderink M, Scotter EL, Oldfield RL, Bergin PS, Mee EW, Graham ES, Faull RLM, Curtis MA, Park TI-H et al (2016) TGF-beta1 regulates human brain pericyte inflammatory processes involved in neurovasculature function. *J Neuroinflammation* 13: 37
- Saunders N, Liddelow S, Dziegielewska K (2012) Barrier mechanisms in the developing brain. *Front Pharmacol* 3: 46
- Shweiki D, Itin A, Soffer D, Keshet E (1992) Vascular endothelial growth factor induced by hypoxia may mediate hypoxia-initiated angiogenesis. *Nature* 359: 843–845
- Silverman JL, Yang M, Lord C, Crawley JN (2010) Behavioural phenotyping assays for mouse models of autism. *Nat Rev Neurosci* 11: 490–502
- Stein I, Itin A, Einat P, Skaliter R, Grossman Z, Keshet E (1998) Translation of vascular endothelial growth factor mRNA by internal ribosome entry: implications for translation under hypoxia. *Mol Cell Biol* 18: 3112–3119
- Sweeney MD, Zhao Z, Montagne A, Nelson AR, Zlokovic BV (2019) Blood-brain barrier: from physiology to disease and back. *Physiol Rev* 99: 21–78
- Torrey EF, Hersh SP, McCabe KD (1975) Early childhood psychosis and bleeding during pregnancy. A prospective study of gravid women and their offspring. *J Autism Child Schizophr* 5: 287–297
- Vasudevan A, Long JE, Crandall JE, Rubenstein JLR, Bhide PG (2008) Compartment-specific transcription factors orchestrate angiogenesis gradients in the embryonic brain. *Nat Neurosci* 11: 429–439
- Via DP, Plant AL, Craig IF, Gotto AM, Smith LC (1985) Metabolism of normal and modified low-density lipoproteins by macrophage cell lines of murine and human origin. *Biochim Biophys Acta - Lipids Lipid Metab* 833: 417–428
- Virgintino D, Girolamo F, Errede M, Capobianco C, Robertson D, Stallcup WB, Perris R, Roncali L (2007) An intimate interplay between precocious, migrating pericytes and endothelial cells governs human fetal brain angiogenesis. *Angiogenesis* 10: 35–45
- Werling DM, PARIKSHAK NN, Geschwind DH (2016) Gene expression in human brain implicates sexually dimorphic pathways in autism spectrum disorders. *Nat Commun* 7: 10717
- Winkler EA, Bell RD, Zlokovic BV (2011) Central nervous system pericytes in health and disease. *Nat Neurosci* 14: 1398–1405
- Winkler EA, Sengillo JD, Bell RD, Wang J, Zlokovic BV (2012) Blood-spinal cord barrier pericyte reductions contribute to increased capillary permeability. *J Cereb Blood Flow Metab* 32: 1841–1852
- Wu Y, Li X, Liu J, Luo X-J, Yao Y-G (2020) SZDB2.0: an updated comprehensive resource for schizophrenia research. *Hum Genet* 139: 1285–1297
- Yao L, Xue X, Yu P, Ni Y, Chen F (2018) Evans blue dye: a revisit of its applications in biomedicine. *Contrast Media Mol Imaging* 2018: 7628037
- Zacchigna L, Vecchione C, Notti A, Cordenonsi M, Dupont S, Maretto S, Cifelli G, Ferrari A, Maffei A, Fabbro C et al (2006) Emilin1 links TGF- $\beta$  maturation to blood pressure homeostasis. *Cell* 124: 929–942
- Zhao Q, Dai W, Chen HY, Jacobs RE, Zlokovic BV, Lund BT, Montagne A, Bonnin A (2022) Prenatal disruption of blood-brain barrier formation via cyclooxygenase activation leads to lifelong brain inflammation. *Proc Natl Acad Sci U S A* 119: e2113310119



**License:** This is an open access article under the terms of the [Creative Commons Attribution-NonCommercial-NoDerivs](https://creativecommons.org/licenses/by-nc-nd/4.0/) License, which permits use and distribution in any medium, provided the original work is properly cited, the use is non-commercial and no modifications or adaptations are made.